



**AFRL-OSR-VA-TR-2013-0347**

## **Ceramics for High Power Lasers**

**R.L. Byer, R.M. Gaume, R.K. Route, C. Rudy**  
**Stanford University**

**July 2013**  
**Final Report**

**DISTRIBUTION A: Approved for public release.**

**AIR FORCE RESEARCH LABORATORY**  
**AF OFFICE OF SCIENTIFIC RESEARCH (AFOSR)**  
**ARLINGTON, VIRGINIA 22203**  
**AIR FORCE MATERIEL COMMAND**

REPORT DOCUMENTATION PAGE				Form Approved OMB No. 0704-0188	
Public reporting burden for this collection of information is estimated to average 1 hour per response, including the time for reviewing instructions, searching existing data sources, gathering and maintaining the data needed, and completing and reviewing this collection of information. Send comments regarding this burden estimate or any other aspect of this collection of information, including suggestions for reducing this burden to Department of Defense, Washington Headquarters Services, Directorate for Information Operations and Reports (0704-0188), 1215 Jefferson Davis Highway, Suite 1204, Arlington, VA 22202-4302. Respondents should be aware that notwithstanding any other provision of law, no person shall be subject to any penalty for failing to comply with a collection of information if it does not display a currently valid OMB control number. PLEASE DO NOT RETURN YOUR FORM TO THE ABOVE ADDRESS.					
1. REPORT DATE (DD-MM-YYYY) 05-15-2013		2. REPORT TYPE Final Performance Report to: Dr. Howard Schlossberg, AFOSR/RSE		3. DATES COVERED (From - To) 05-15-2010 to 05-15-2013	
4. TITLE AND SUBTITLE Ceramics for High Power Lasers				5a. CONTRACT NUMBER	
				5b. GRANT NUMBER FA9550-10-1-0227	
				5c. PROGRAM ELEMENT NUMBER	
6. AUTHOR(S) R.L. Byer, R.M. Gaume, R.K. Route, C. Rudy				5d. PROJECT NUMBER	
				5e. TASK NUMBER	
				5f. WORK UNIT NUMBER	
7. PERFORMING ORGANIZATION NAME(S) AND ADDRESS(ES) Edward L. Ginzton Laboratory Stanford University Stanford, CA 94305-4088				8. PERFORMING ORGANIZATION REPORT NUMBER SPO No. 49850	
9. SPONSORING / MONITORING AGENCY NAME(S) AND ADDRESS(ES) AFOSR 875 North Randolph Street, Room 3112 Arlington, VA 22203				10. SPONSOR/MONITOR'S ACRONYM(S)	
				11. SPONSOR/MONITOR'S REPORT NUMBER(S) AFRL-OSR-VA-TR-2013-0347	
12. DISTRIBUTION / AVAILABILITY STATEMENT Approved for public release; distribution unlimited.					
13. SUPPLEMENTARY NOTES The view, opinions and/or findings contained herein are those of the author(s) and should not be construed as necessarily representing the official policies or endorsements, either expressed or implied, of the Air Force Office of Scientific Research or the U.S. Government.					
14. ABSTRACT <p>Transparent ceramic gain-media can lead, when properly engineered, to significant improvements in solid-state laser performance. Among the anticipated benefits of such material-based lasers are high-average power outputs with higher efficiencies, improved pulse-energy storage and outputs, higher ultrafast-laser performance, and phased-array operation of guided-wave laser systems. In this research program we focused on the application, design and testing of engineered laser ceramics. We worked on (1) the study of bulk defects in YAG ceramics; (2) a efforts to fabricate bulk transparent ceramics of YAG with improved optical quality; and (3) the design and fabrication of waveguide structures based on theoretical predictions of laser host performance and composite laser design. The dual focus on correlating processing parameters with both performance and optical losses was taken to achieve high quality ceramics along with a fundamental understanding about these materials at all levels of manufacturing and use.</p> <p>In the final two years, we undertook the study of technologies to produce high power, two-micron fiber lasers because of their eye-safe characteristics and importance to military applications.</p>					
15. SUBJECT TERMS Ceramic laser, high energy laser, transparent ceramics, engineered ceramics, transparent polycrystalline material					
16. SECURITY CLASSIFICATION OF:			17. LIMITATION OF ABSTRACT	18. NUMBER OF PAGES  36	19a. NAME OF RESPONSIBLE PERSON Robert L. Byer
a. REPORT	b. ABSTRACT	c. THIS PAGE			19b. TELEPHONE NUMBER (include area code) (650) 723-0226

SF 298 Continuation Sheet  
Interim Performance Report to Dr. Howard Schlossberg, AFOSR/RSE

1. AFOSR GRANT NUMBER: FA9550-10-1-0227
2. PERIOD COVERED BY REPORT: 05-15-2010 to 05-15-2013
3. TITLE OF PROPOSAL: Ceramics for High Power Lasers
4. LIST OF MANUSCRIPTS SUBMITTED OR PUBLISHED UNDER AFOSR SPONSORSHIP DURING THIS REPORTING PERIOD:

See attached report

5. SCIENTIFIC PERSONNEL SUPPORTED BY THIS PROJECT AND DEGREES AWARDED DURING THIS REPORTING PERIOD:

Faculty - R. L. Byer

Staff - R. M. Gaume, R.K. Route, A. Markosyan

Graduate Students – C. Rudy, S. Wolf

6. REPORT OF INVENTIONS BY TITLE ONLY:
7. SCIENTIFIC PROGRESS AND ACCOMPLISHMENTS: See Interim Performance Report
8. TECHNOLOGY TRANSFER:

This program explores micro-structured ceramic materials for use as transparent laser host materials to replace crystalline laser host materials. It also explores avenues toward high power two-micron fiber lasers. Technology developed under this program will be available through Stanford's Office of Technology and Licensing.

9. CORRESPONDENCE ADDRESS:

Robert L. Byer, P.I.

Ginzton Laboratory, Mail Code 4088

Stanford University

Stanford, CA 94305-4088

(tel) 650-723-0226

(fax) 650-723-2666

byer@stanford.edu

**Final Performance Report**  
**on**  
**Ceramics for High Power Lasers**  
**(FA9550-10-1-0227)**  
**for the period**  
**05/15/2010 through 05/15/2013**  
  
**Ginzton Lab, Stanford University**  
**Robert L. Byer (P.I.)**

## **I. Introduction**

The present document combines the third Annual Performance Reports with the final technical report on our research program on ceramics for high-power lasers and technology for high power two-micron fiber lasers.

The objectives of this 36-month program under AFOSR support, FA9550-10-1-0227, are:

1. The continued study of bulk defects in YAG ceramics;
2. A continuation of efforts to fabricate bulk transparent ceramics of YAG with improved optical quality; and
3. The design and fabrication of waveguide structures based on theoretical predictions of laser host performance and composite laser design.
4. Development of technology leading to a high power, two-micron fiber laser.

These four basic research goals build upon prior accomplishments under FA9550-07-1-0392 and greatly expand our knowledge of the origin of optical losses in ceramic laser host materials while initiating a program of research on 2-micron, thulium-doped fiber laser technology.

## **II. Technical Report**

Our current research effort encompasses materials synthesis studies, materials analysis and laser device characterization in a fully-integrated vertical program model that has historically been very successful at Stanford. The objective is to establish a fundamental understanding of how ceramic YAG laser host can be designed to yield laser components with superior laser performance. Using expertise in transparent ceramics fabrication, micro-scale optical characterizations, laser design and laser testing, we have sought to advance the fundamental knowledge about engineered gain media for high-power laser materials.

In the long term, we are interested in designing test structures for improved laser efficiency at high-power and developing algorithms to solve the inverse diffusion problem for creating desired dopant concentration profiles. We have focused to date on parabolic and hyperbolic dopant concentration profiles in transparent optical ceramics. This work necessitated an in-depth understanding of dopant diffusion to control gain and loss in engineered gain-media and it

required the development of specific ceramic processing methodologies to achieve precise spatial control of dopants in the host, both of which were addressed during the prior program.

Toward the end of Year 1, the ceramic fabrication effort was relocated from Stanford to the University of Central Florida (UCF) following Dr. Romain Gaume's appointment as a faculty member there. At the same time, virtually all of the ceramic materials fabrication equipment then in use was relocated to UCF. At this writing, we are still awaiting its installation and commissioning at UCF. This shuffling of people and equipment caused a temporary suspension of the ceramics fabrication efforts at Stanford and in the interim we have focused on the study of bulk defects in YAG ceramics. We anticipate that our original efforts on ceramic fabrication will continue at UCF sometime in the near future, launched with subcontract support from our subject program, and continuing thereafter with independent agency funding.

## Accomplishments

### *I. Study of bulk defects in YAG ceramics*

During Year 1 of this program, we produced and characterized laser grade Nd:YAG and low optical loss  $Gd^{3+}$  doped YAG and Tm:YAG ceramics. Laser performance remained limited by residual scattering in our ceramic Nd:YAG, however.

We carried out comparative studies on different YAG powders and powder forming techniques followed by the fabrication of transparent YAG ceramics by vacuum sintering. This work motivated a specific study on the influence of chemical composition on the transparency of YAG ceramics. This approach not only helped us to obtain better consistency in our fabrication process but also led to new developments in the role played by point defects in non-stoichiometric YAG. This work focused primarily on departures from stoichiometry was fully reported in the final technical report under our previous program, FA9550-07-1-0392.

Our main efforts were on elucidating the effects of silicon, which is introduced as  $SiO_2$  to act as a sintering aid to minimize internal voids during high temperature vacuum sintering. High sensitivity optical absorption at 1  $\mu m$  was measured in forty undoped and Nd-doped YAG ( $Y_3Al_5O_{12}$ ) transparent ceramics and single crystals using photothermal common-path interferometry (PCI). Concurrently, chemical trace analysis was performed on those samples by Glow Discharge Mass-Spectroscopy (GDMS). Silicon and calcium were found to be the major impurities with concentrations up to 250 ppm wt. A linear correlation between the Si content and the absorption loss at 1  $\mu m$  was revealed and a possible mechanism for the formation of Si-induced color centers based on a bound polaron model was considered, and solutions to reduce this absorption in ceramics were developed. This work has formed the basis of our most recent publication, "Effect of Si-induced Defects on 1  $\mu m$  Absorption Losses in Laser-Grade YAG Ceramics" by authors Y.He, R.Gaume, A.Markosyan, and R.L.Byer, J Appl. Phy. **111**, 093104 (2012). A manuscript version is appended to this report.

### *Progress on the design of engineered ceramic gain media*

The results from our prior investigations into micro-engineered ceramic structures have provided several critical insights. First, the length scale of possible doping profiles can be characterized by

measuring the distance over which the doping level falls to  $1/e$  its initial value, referred to as  $L$ , the diffusion length. Multiplying this distance by two is a measure of the minimum width achievable in engineered doping profiles. Accordingly, the measurements of Nd-diffusion distances in reactively sintered ceramics demonstrate that the smallest width for state-of-the-art reactive-sintered interfaces is in the neighborhood of 500 microns. The most critical variables controlling the production of much smaller profile widths ( $\sim 10$  microns) are the materials systems chosen and the details of the processing conditions used. In addition, it is important to determine how great a reduction in laser performance is suffered when layer thicknesses are significantly greater in size.

#### Processing conditions for 10 $\mu$ m wide doping profiles

Trade-offs have been found between sintering time and temperature on the overall transparency of a ceramic material and the distance doping ions are expected to travel by diffusion during processing. If a ceramic is sintered at a low temperature for a short time, for example, the dopant ions are not expected to travel very far. However, the optical quality of the ceramic can be expected to suffer because at low temperatures and times the pores within the ceramic are not able to collapse, leaving scattering centers. We performed measurements of the diffusion distances of Nd ions in fully densified (transparent) ceramics and for different sintering times and temperatures. This allowed us to determine the maximum processing time and temperature for 10 $\mu$ m -wide profiles.

The variation of the diffusion length with sintering time,  $t$ , and sintering temperature  $T$ , was experimentally shown to follow,

$$L = \frac{t^{3/10}}{\exp(E/(RT) - A)},$$

where  $E$  is an experimentally determined activation energy with a value of 310  $\pm$  30 kJ/mol,  $R$  is the ideal gas constant and  $A$  is a constant with a value of 21.92 using units of microns/hour. According to the measurements, if the initial nanoparticles are larger than 200nm, 10-micon-wide doping profiles can be fabricated by sintering at 1650°C, for up to 200 hours. There is a greater potential for small doping profiles with single-phase sintering techniques, rather than reactive sintering.

#### Centimeter-scale doping profiles for laser applications

Doping profiles with 1-cm-and-larger widths are readily achievable with current ceramic processing techniques. One application for doping profiles is to simplify edge pumping of slab lasers by clustering more dopant in the center of the gain medium where it can be easily extracted by a TEM<sub>00</sub> optical field. The figure below shows the relevant geometry. For base-lining standard edge-pumped lasers, a gain medium with a uniform doping profile was modeled. This result was more power being absorbed at the edges of the gain medium which makes it difficult to extract the energy from the excited dopant atoms in these regions. Clustering more dopant in the center of the slab allows the slab to operate more efficiently with TEM<sub>00</sub> beams.

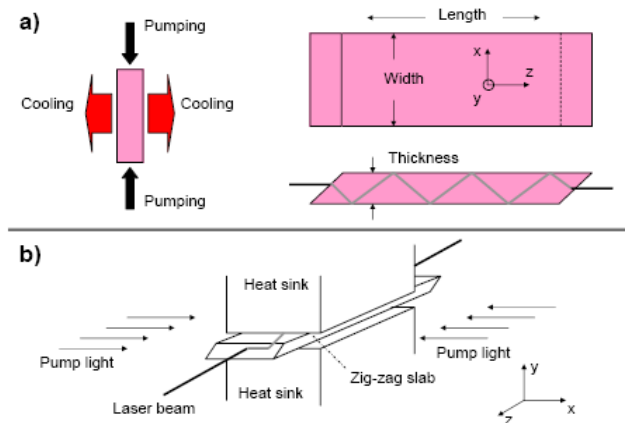


**Fig. 7** End-pumped (top) and edge-pumped (bottom) geometries

There is a complication that comes with changing the doping level of gain ions: as the doping level is varied, the refractive index also changes. Refractive index variations from doping profiles can distort TEM<sub>00</sub> beams, eliminating the advantage of more efficient pumping and extraction. Therefore, the doping profile used must be carefully considered, so that it both improves extraction but does not result in large beam distortions. Using a genetic algorithm, we determined a doping profile that was able to improve wall-plug efficiency for an edge-pumped Nd:YAG slab by 39% over an optimally designed uniformly doped slab. The resulting profile is shown below.

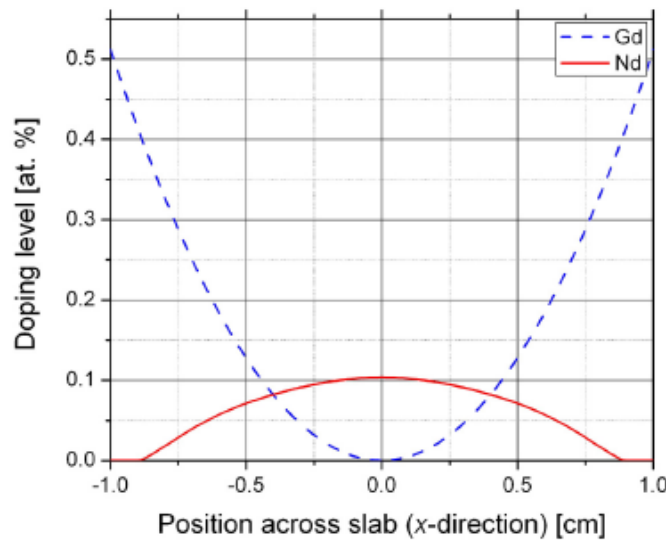


**Fig. 8** Calculated Nd<sup>3+</sup> and Gd<sup>3+</sup> doping concentrations in the cross-section of a laser slab optimized for edge-pumping operation.

We produced ceramic composites (Fig.9) at Stanford with simple Nd<sup>3+</sup> and Gd<sup>3+</sup> profiles and carried out optical characterizations. Laser-scanning confocal microscopy was used to measure the spatial distribution of Nd<sup>3+</sup> ions by fluorescence detection. Confocal microscopes offer high spatial resolution at laser wavelengths by combining a tightly focused laser beam with a confocal imaging system. In Fig.10 (a), at each point, a fluorescence spectrum is recorded. The fluorescence intensity at 885nm considered to be 1% Nd doped and the darker point is 0% Nd<sup>3+</sup>

doped. The scanning images in Fig. 10 (b), (c), (d), clearly showed the larger diffusion of  $\text{Nd}^{3+}$  along grain boundaries than lattice. The doping profiles (Fig. 11) were calculated from maps in Fig.10 by taking the average intensity on sections parallel to the interface. The diffusion length of  $\text{Nd}^{3+}$  increased as heating time increases, and appeared to saturate at  $20\mu\text{m}$  after 92 hours of heating.

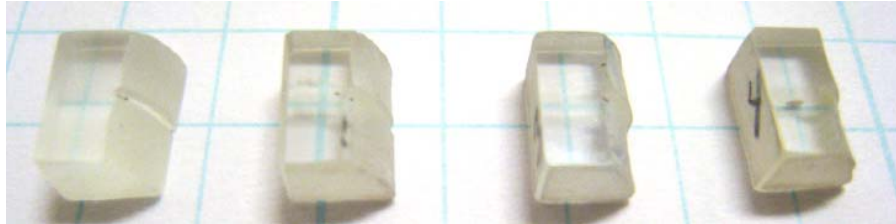


**Fig. 9**  $\text{Nd}^{3+}$ ,  $\text{Gd}^{3+}$ :YAG ceramic composites made at Stanford by thermal bonding. Samples are 7 mm long and are laser grade.

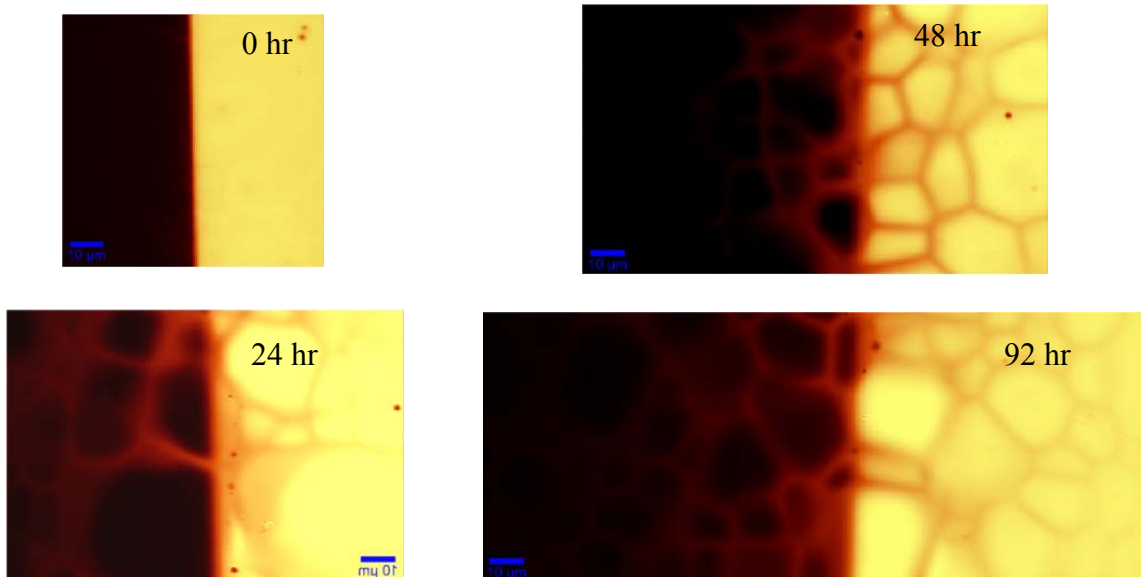


**Fig. 10** Scanning confocal microscope spectroscopy images of bonded Nd:YAG (right side) and Gd:YAG (left side) annealed at 1700C for 0hr, 24hrs, 48hrs and 92hrs, respectively. (Scale bar =  $10\mu\text{m}$ )



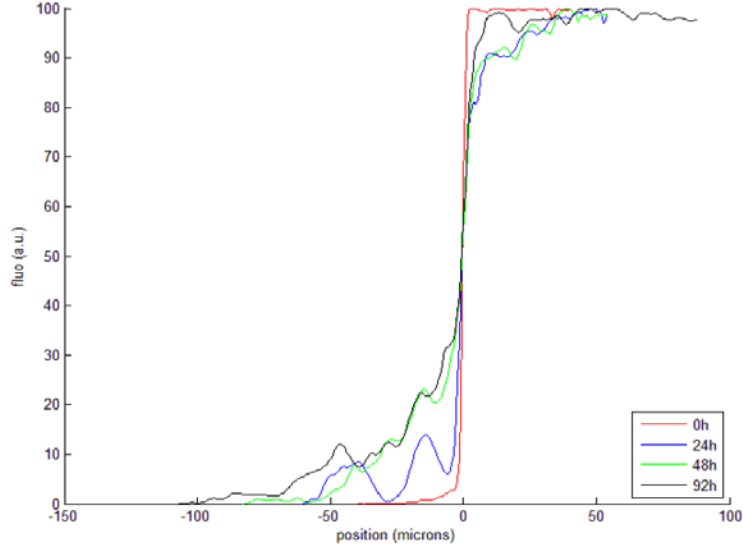


**Fig. 11** Dopant profile of bonded Nd:YAG (right side) and Gd:YAG (left side) annealed at 1700C for 0hr, 24hrs, 48hrs and 92hrs.

In a study to verify that gadolinium doping can indeed be used to compensate for the change of refractive index induced by the gradient of neodymium concentration, we measured the wave-front distortion of a He-Ne laser beam (633nm) perpendicular to the bonded interface of a 1at% Nd:YAG||1at% Gd:YAG bonded ceramic sample. A wave-front sensor (Schack-Hartmann) was used for this measurement. The recorded phase is shown in Fig.12 which shows an average phase difference of around  $10^{-7}$  across the bonded interface. This phase shift corresponds to an estimated value of  $6 \times 10^{-5}$  for the difference in refractive index between the two sides of the bond. This value compares reasonably well with the expected index difference  $\Delta n \sim 3 \times 10^{-5}$  between Nd:YAG and Gd:YAG obtained from literature. These phase-sensitive measurements will need to be refined and confirmed in future studies.

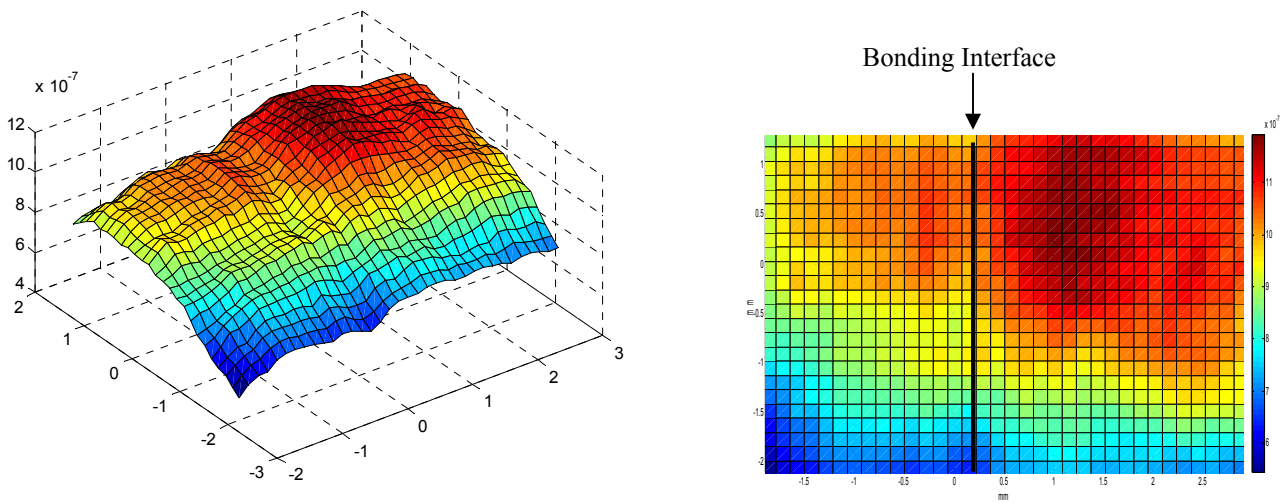


**Fig. 12** Phase distortion of a planar laser wavefront propagating perpendicular to a bonded Nd:YAG||Gd:YAG interface.

### *Progress on the characterization of low-loss laser ceramics*

We also invested effort in developing instrumentation to better evaluate optical losses in high quality transparent ceramics and provide guidance for improving the ceramic fabrication process. We previously characterized three ceramic slabs produced at the World-Lab. Co. Ltd. Nagoya, Japan. The slabs (6x10x75mm) were polished on all sides (Fig.13). In most instances, these samples have been compared with a 1 at% Nd:YAG single-crystal and a 1 at% Nd:YAG ceramic purchased from Scientific Materials and Konoshima Corp. respectively.

**Table 1** Samples tested

<b>Material</b>	<b>Origin</b>	<b>Sample reference #</b>
Undoped YAG ceramic	Ikesue	Z-713
1 at% Nd:YAG ceramic	Ikesue	Z-714
1 at% Gd:YAG ceramic	Ikesue	Z-715
1 at% Nd:YAG ceramic	Konoshima	Kono1
1 at% Nd:YAG single crystal	Scientific Materials	Sc1

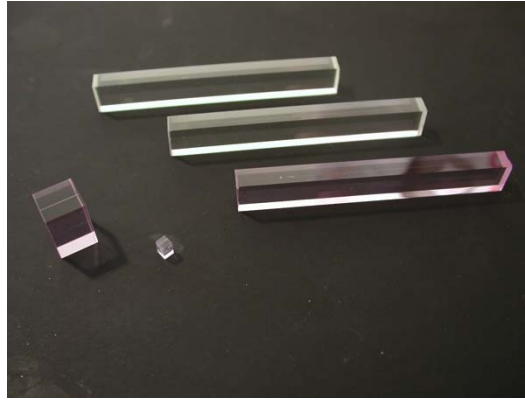


**Fig. 13** Transparent ceramic slab of YAG, Nd<sup>3+</sup>:YAG and Gd<sup>3+</sup>:YAG. The Konoshima (10x10x20 mm) and single-crystal (3x3x5mm) test samples are on the left.

Absorption spectroscopy, thermalized absorption, light scattering tomography were used to quantify the absorption and scattering losses in all samples. In addition, confocal laser-gain scanning microscopy as well as laser tests were performed with Nd doped YAG ceramics.

#### Absorption Spectroscopy

The optical quality of ceramic samples was evaluated over a broad wavelength range. A Cary 500 spectrometer with double-beam transmission was used to measure the absorption coefficient in NIR-Vis-UV range (175-2000nm). The absorption coefficient  $\alpha$  was calculated according to the equation:

$$\frac{I}{I_o} = 10^{-OD} = (1 - R)^2 \exp(-\alpha L) \quad (1)$$

Where  $I_o$  and  $I$  are the intensities of the incident and transmitted light, O.D is the optical density measured by the spectrophotometer,  $R$  is the Fresnel reflection at normal incidence per interface, and  $L$  is the sample thickness.

We first verified that, in the Nd doped sample, the linear absorption coefficient at 808 nm was consistent with a 1 at% doping level. We also found that the absorption spectra of the undoped and Gd-doped YAG samples exhibit absorption peaks characteristic of a luminescent rare-earth contaminant (Fig 14). The superimposition of these spectra with the Z-714 one strongly suggested a neodymium contamination in these two other samples. This contamination likely originated from the ball-milling operation where the same jar has been used to process the various compositions.

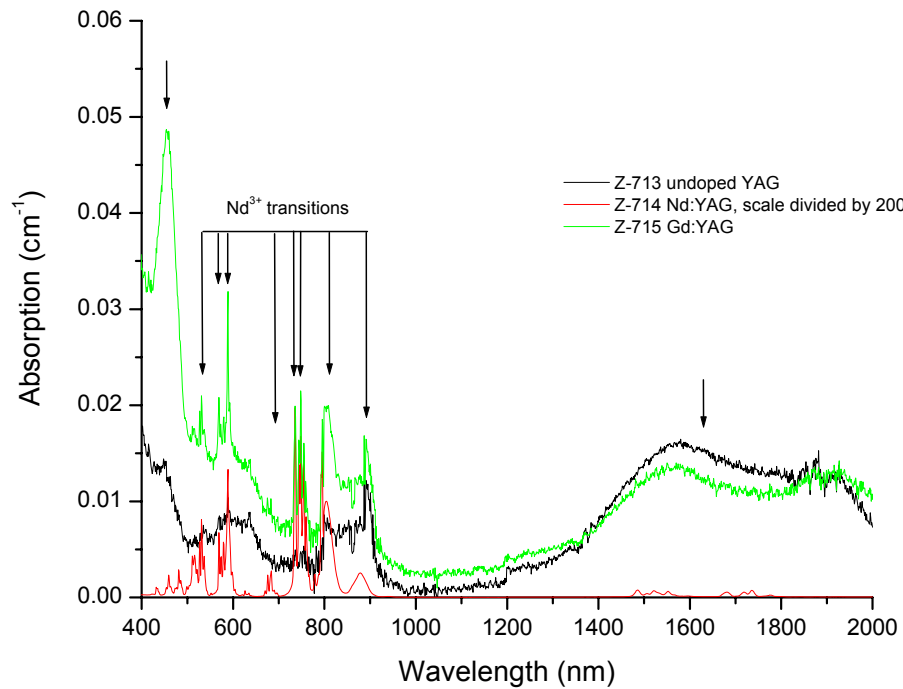


**Fig. 14** Comparison of Z-713, Z-714, Z-715 absorption spectra in the absorption range of Nd<sup>3+</sup>.

Based on linear absorption coefficient measurements, we estimated neodymium impurity levels around 30 ppm and 60 ppm in Z-713 and Z-715 respectively. In addition, three broad and intense absorption bands centered at 457 nm, 1550 and 1900 nm were observed in the undoped and Gd-doped samples. The latter two bands overlapped with absorption lines of the  $^4I_{9/2}-^2I_{15/2}$  transitions but are more intense and broader. This suggested contamination by transition ions.

In comparison, the absorption of Z-714 is plotted in Fig. 15 against the absorption of a Kono1 and Sc1. Z-714, SC1 and Kono1 all exhibited the same features in their absorption spectra. One can notice however that the absorption edge near band-gap ( $\lambda < 300$  nm) increased more dramatically in Z-714 than in the other two test samples. This excess attenuation was attributed to light scattering from residual porosity.

The three ceramic slabs Z-71X presented good optical quality with transmission values reaching the Fresnel limit. However, conventional absorption spectroscopy was not well suited to accurately measure low absorption levels. Therefore, we used the thermalized absorption technique to better quantify absorption losses in these samples.

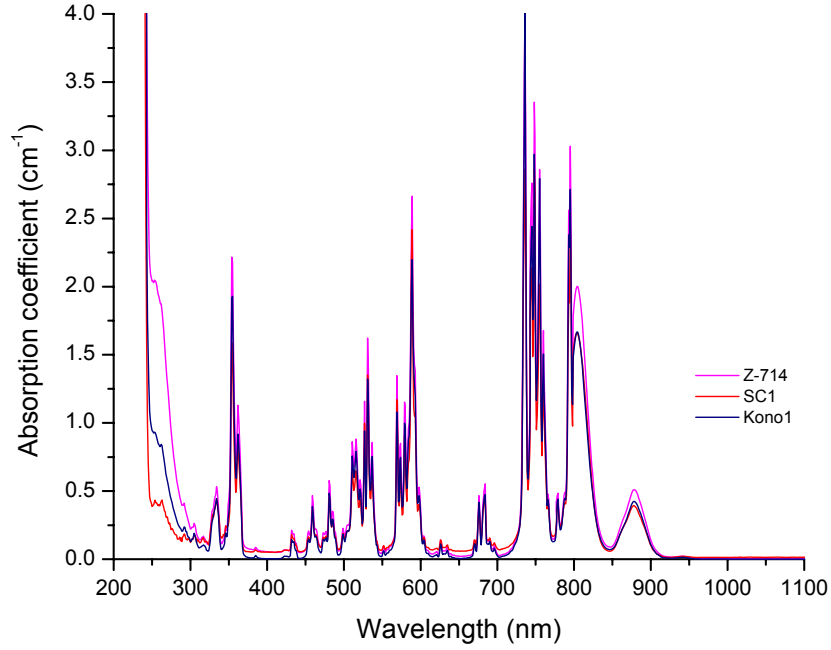


**Fig. 15** Comparison of the absorption spectra of Z-714, Kono1, SC1.

#### Thermalized absorption

Thermalized absorption measurements were made using a photothermal common-path interferometer (PCI). This method was developed at Stanford to measure low absorption levels in bulk optical materials. The principle of this technique is illustrated in Fig. 16. A powerful laser of wavelength  $\lambda$  is tightly focused on the sample. If the material is absorbing at this wavelength, heat will be generated and create a thermal lens. This lens is probed by interferometry using a second probe laser at a different wavelength. The phase shift introduced by this lens is given by:

$$\Delta\varphi = kL \frac{\partial n}{\partial T} \Delta T$$

where  $k$  is the wavevector of the probe laser,  $L$  is the sample thickness,  $\Delta T$  is the temperature increase induced by the pump laser, and  $\partial n / \partial T$  is the thermo-optic coefficient of the material.

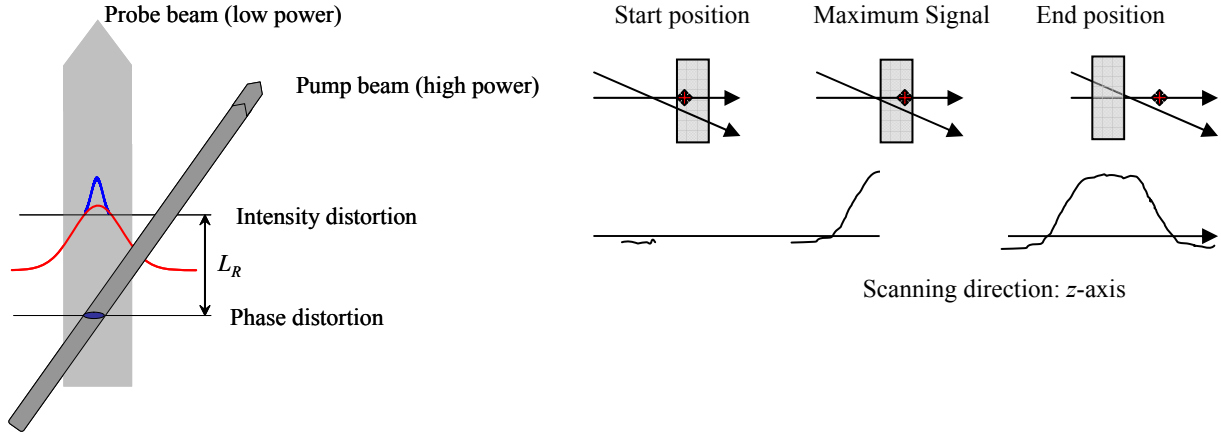


**Fig. 16** PCI Method (left) and measurement technique (right)

Generally, this method can measure absorption levels down to 0.1 ppm/cm. In the present characterization studies, the absorption measurements were obtained at a pump wavelength of 1064 nm. The beam sizes of the probe and pump lasers were 240 $\mu$ m and 70 $\mu$ m, respectively. Individual scattering defects smaller than 40 $\mu$ m in size cannot be spatially resolved. The data obtained with this set-up have been calibrated against high-quality fused silica and sapphire absorption standards having absorptions of 10 and 100 ppm/cm respectively.

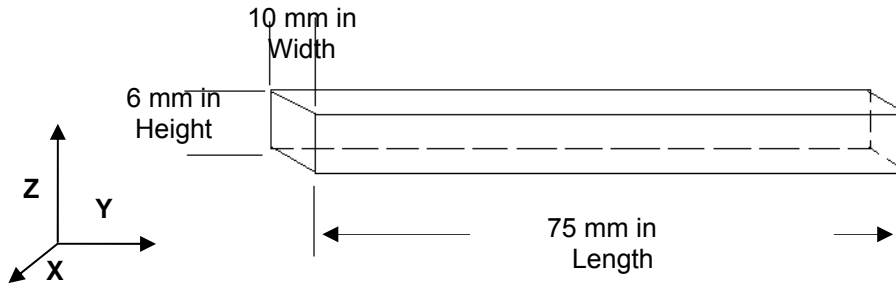


**Fig. 17** Configuration of the (PCI) scan measurements on a slab sample

Scans performed through the entire thickness of the three ceramic slabs (Z- direction on Fig. 17) are plotted in Fig.18 and reveal the evolution of the thermalized absorption within the bulk of the samples. All samples had absorption levels on the order of 1000 ppm/cm. These values were comparable to absorption levels that we measured in the Nd:YAG single-crystal SC1 (Table 2). It is interesting however to note that the Nd and Gd doped samples had significantly higher absorption levels than the undoped ceramic (Table 2). In Fig.18, the peaks appearing on both sides of the samples result from surface absorption and are not accounted for in the average bulk absorption. The small symmetric peaks located outside the Nd-doped sample result from interference of the two laser beams.

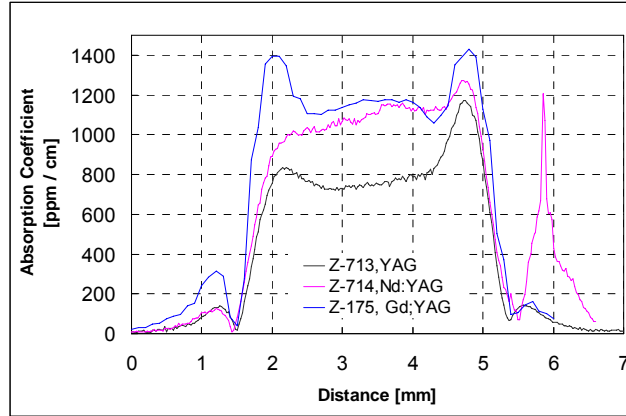


**Fig. 18** Thermalized absorption at 1064nm for the Z-713, Z-714 and Z-715 samples

**Table 2** Average values of the thermalized absorption coefficients in the investigated samples

Absorption Coefficient (ppm/cm)	
YAG, Z-713	750
Nd:YAG, Z-714	1050
Gd:YAG, Z-715	1100
Single-crystal Sc1	1000
Kono1	135
Fused silica standard	10
Sapphire standard	100

Figure 19 shows two scans performed at constant depth and along the largest dimension of the Nd doped and Gd doped YAG slabs (Y-direction on Fig. 17). In the case of the Gd:YAG sample, sharp spikes occasionally appeared during the scan (Fig. 19a). These spikes were associated with large phase jumps between the two arms of the common-path interferometer and drops in the transmitted pump power. The corresponding features can be unambiguously attributed to light scattering on pores. The size of these pores is estimated to be in the 100-300  $\mu\text{m}$  range. In the Gd:YAG sample, the density of scatterers detected by this technique was approximately  $1.36 \times 10^5 \text{ cm}^{-3}$  which corresponded to a pore volume fraction of 0.06 ppb. Some larger defects, on the order of 1mm, were also seen in Z-714 (Fig 19b) but at a much lower concentration.

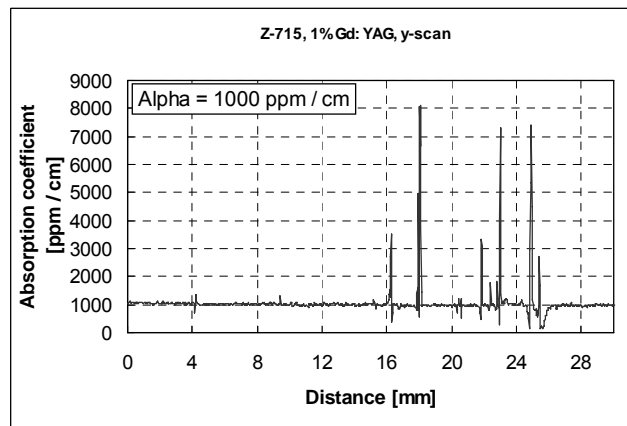


**Fig. 19a** Thermalized absorption at 1064 nm in Z-715

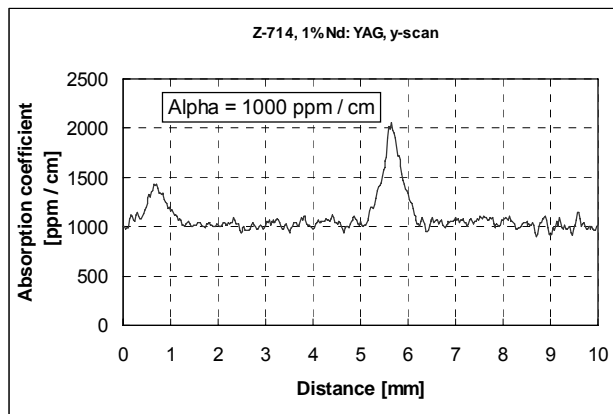


**Fig. 19b** Thermalized absorption at 1064 nm in Z-714

For comparison, Fig. 20 below shows the absorption profile at 1064nm in the ceramic sample purchased from Konoshima. The average absorption in this material was about seven times lower than in the Z-714 and SC1 samples.

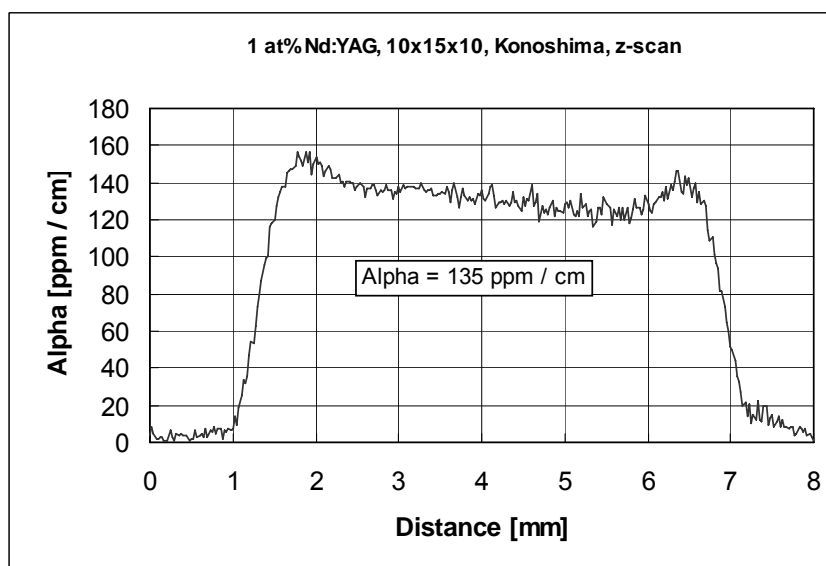


**Fig. 20** Thermalized absorption at 1064nm in the 1 at% Nd:YAG produced by Konoshima Corp.

To understand the difference of absorption in different YAG systems, we conducted PCI measurements on 30 YAG samples, both ceramics and single crystals, both doped and non-doped. Figure 21 illustrates the absorption coefficients of YAG ceramics and single crystals from different vendors.

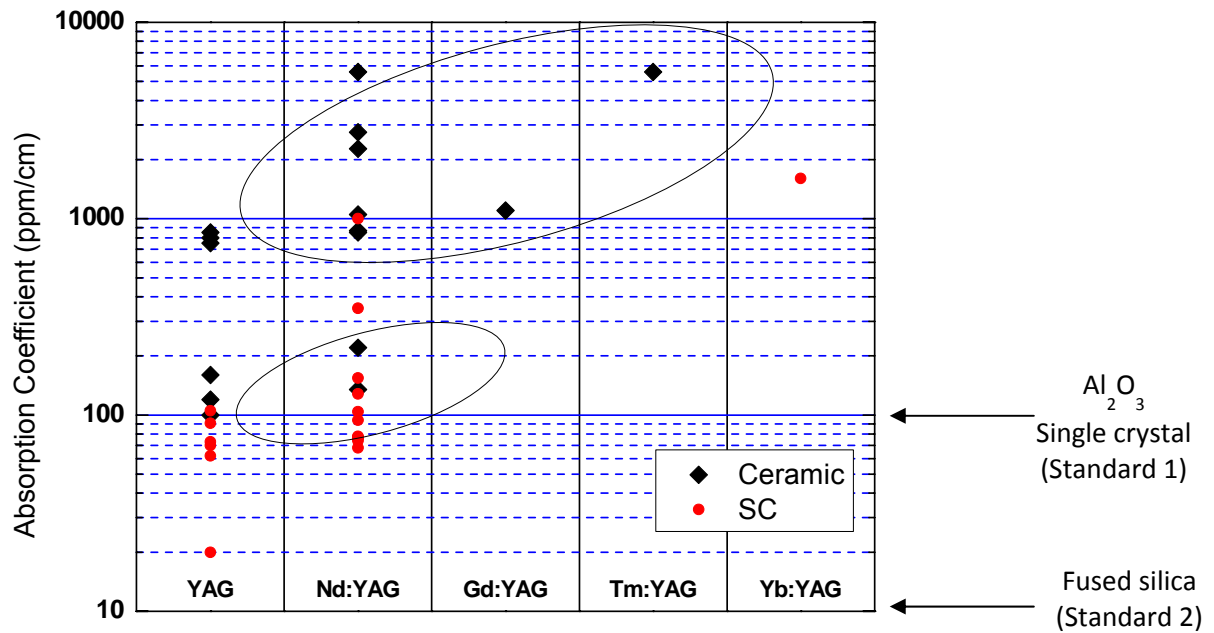


**Fig. 21** Absorption coefficient of non-doped YAG and doped YAG ceramics and single crystals at 1064 nm. The x-axis indicates different chemical composition, and the black and red dots represent ceramics and single crystals, respectively. The top oval includes ceramics (black dots) by reactive sintering, and bottom one includes ceramics by non-reactive sintering.

Figure 21 shows that the absorption coefficient of the various ceramic samples investigated ranged from 100 to 8000 ppm/cm depending on fabrication. It is worth noting that certain ceramic samples have absorption coefficients that rival those of single crystals (~100ppm/cm). From that standpoint, this fact confirms that high quality ceramics are suitable for high power laser gain media. Figure 21 also suggests that reactively sintered YAG ceramics exhibit, on average, absorption coefficients that are one order of magnitude higher than those measured in non-reactively sintered samples. The fact that higher concentrations of  $\text{SiO}_2$  (sintering aid) are typically used in the former process than in the latter has been further investigated as a possible explanation for this observation.

Comprehensive chemical analysis was performed by Evans Analytical Group (EAG) using inductively coupled plasma mass spec. analysis (ICP-MS) on 25 elements ranging from transition metals, rare earths, alkali, alkaline earths and silicon on a set of selected YAG ceramics and single crystals samples. It was found that, for all samples, the major contaminants were silicon and calcium. The fact that the absorption coefficient in YAG samples correlates with the silicon concentration (and to a lesser extent the calcium concentration) suggests that color centers associated with these ions may contribute to the 1064 nm absorption, as suggested by Fig. 22. Further investigation on defect formation will still be needed to clarify this phenomenon and help improve the fabrication of low absorption YAG ceramic materials.



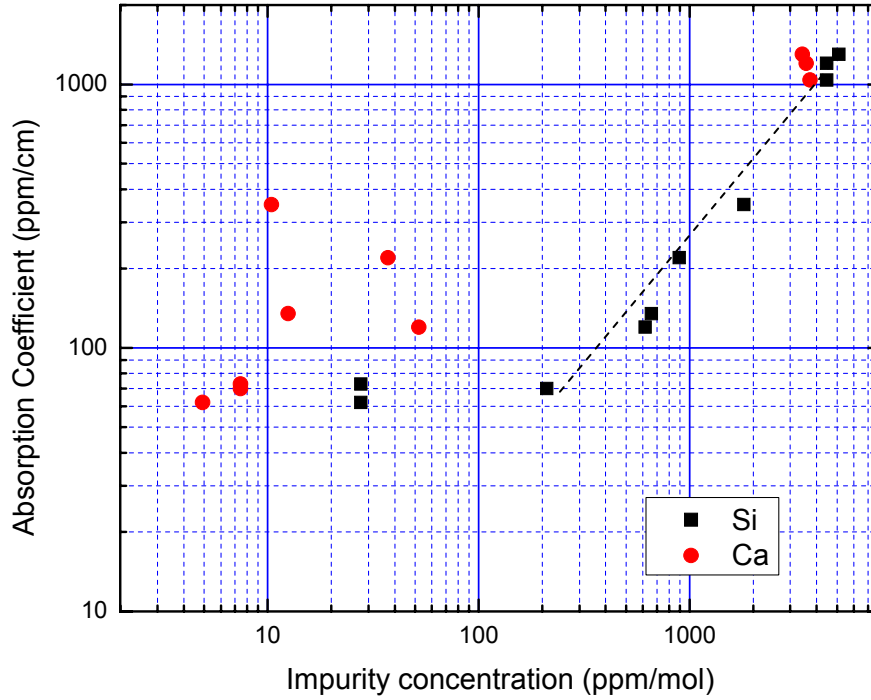


**Fig. 22** The concentration of impurity  $\text{Si}^{4+}$  and  $\text{Ca}^{2+}$  in different samples with different absorption coefficients (Black squares denote  $\text{Si}^{4+}$ , and red circles denote  $\text{Ca}^{2+}$ , while the dashed line is the linear fit on a log scale.)

### Confocal Laser-Gain Scanning Microscopy

We developed a confocal laser-gain scanning microscope to accurately measure material transmission at a specific laser signal wavelength. This technique simultaneously measures dopant concentration with high-spatial resolution and high dynamic range from ppm levels to several at%. It also offers a way to compare quantum efficiency between samples. Optical concentration profilometry can be performed by measuring the absorption or gain of the ion of interest with a resolution limited by the size of the probe and/or pump beams. To achieve high spatial resolution, small spot sizes are required. However, the presence of defects in imperfect transparent ceramics, such as secondary phases and pores, can induce large scattering losses for small spot sizes, which can mask the actual absorbed signal. This problem was mitigated by using a probe beam in addition to the pump beam. If the probe beam is significantly larger than the pump beam, this arrangement reduces the influence of material defects on the final measurement without sacrificing spatial resolution of the reconstructed profile. Figure 23 on the following page shows a schematic of a confocal laser-gain scanning microscope.

To measure the dopant concentration, the ceramic was optically pumped with a tightly focused laser beam, which excited the REIs contained in the very small pumped volume. A probe beam

at a wavelength where the excited REIs exhibit gain was launched into the pumped volume and the extracted power was measured. If bleaching is avoided, the REI concentration can be inferred from this measured extracted power. By scanning the ceramic, it was possible to form one- and two- dimensional images of the concentration profile. The setup for our measurements in  $\text{Nd}^{3+}$ :YAG consisted of an amplitude modulated 532 nm pump beam that was focused into the

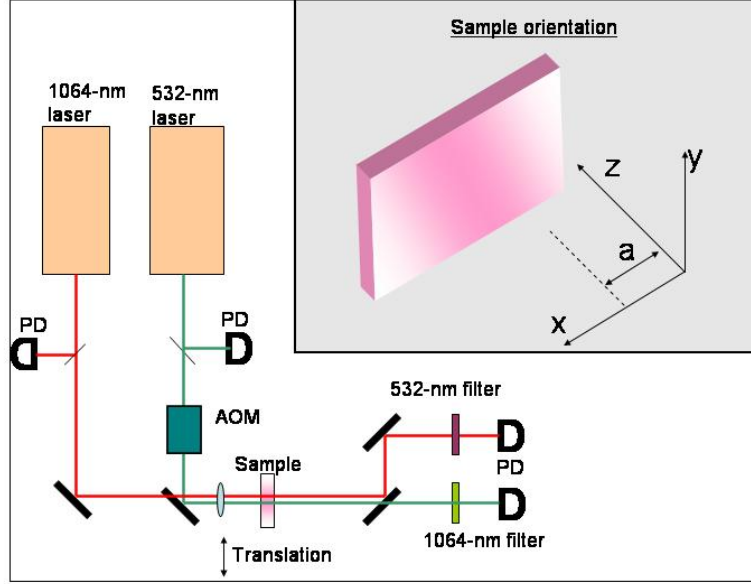


**Fig. 23** Experimental setup of the confocal laser-gain scanning microscope used for the measurement of doping profiles in transparent YAG ceramics. The sample was translated along the  $x$  direction to determine its dopant profile. The inset shows the orientation of the sample relative to the coordinate axis of the laboratory frame. The laser beams propagate in the  $z$  direction, and the profile varies exclusively along the  $x$  direction. AOM: Acousto-optic modulator, PD: Photodiode. The probe laser at 1064 nm has a  $100\mu\text{m}$  beam size and a power of 4 mW. The pump laser at 532nm had a  $250\mu\text{m}$  beam size and a power of 1W.

ceramic. The extracted power at the chopping frequency,  $f$ , was monitored with a 1064 nm probe beam which co-propagated with the 532 nm pump. Through suitable selection of the pump and probe wavelengths this technique can be employed for virtually any laser ceramic gain medium.

In this study, 24 mm-long linear scans were performed on the Nd:YAG Z-714 sample with translation increments of 60 or  $100\mu\text{m}$ . Figure 24 shows the extracted power at 1064 nm in-phase with the modulated pump beam. This extracted power was directly proportional to the concentration of  $\text{Nd}^{3+}$  ions- provided that the quantum efficiency was constant across the sample. Two curves, corresponding to two successive 24mm-scans only overlapping by 2mm, are represented on this plot. The oscillation of the signal was due to temporal instabilities of the probe diode laser source. However the signal fluctuations only represented 0.14% of the signal amplitude. These measurements confirmed that sample Z-714 presented a homogenous gain over the entire slab and that both dopant concentration and fluorescence efficiency were uniform.

Scans were also taken at various positions within the width of the sample, at  $z = 10, 35$  and  $65\text{mm}$  respectively from the top surface of the slab. All these scans are plotted in Fig. 25 and confirm the overall good uniformity of the gain. On this plot, the slight raise of the gain observed near the edge of the slab (for  $z = 65\text{ mm}$ ) is actually an artifact due to the close proximity of the

beam and the slab edge. For an intermediate position ( $z = 35\text{mm}$ ), a few spikes of about  $100\text{ }\mu\text{m}$  width were observed. It was noticed that both pump and probe beams were simultaneously attenuated when passing through these localized regions (Fig. 26). This strongly suggested that these spikes actually corresponded to scattering centers. According to our measurements, the density of scatters was on the order of  $1.25 \times 10^5\text{ cm}^{-3}$ , which is consistent with the estimate obtained from the thermalized absorption technique.

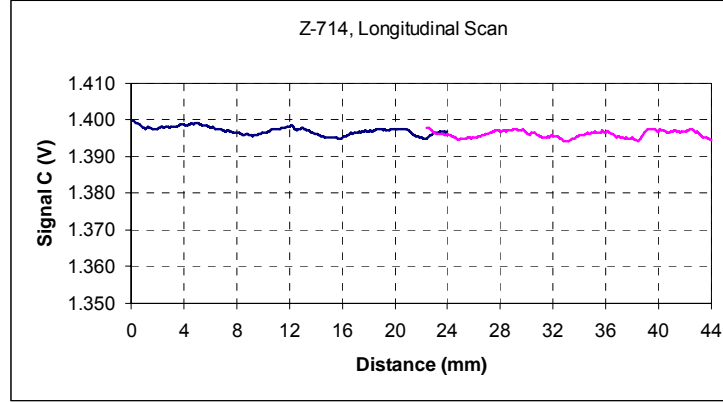


**Fig. 24** Scan of sample Z-714 along the Y-axis near the center of the sample.

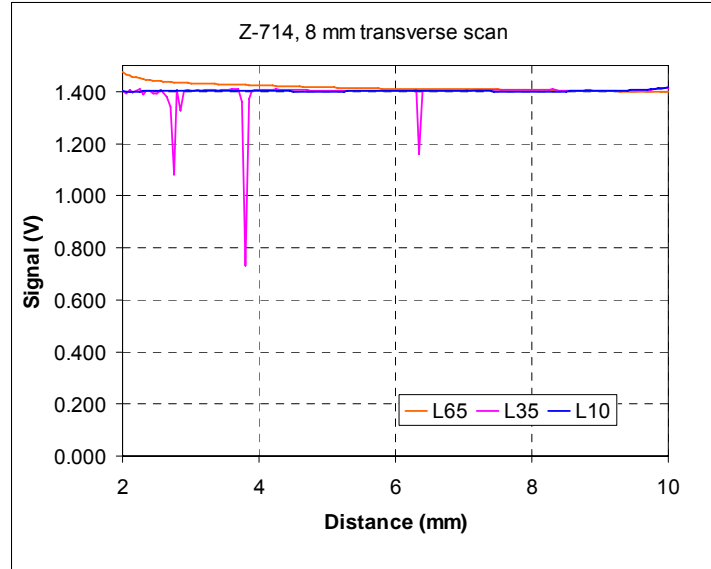


**Fig. 25** Scans of sample Z-714 along the X-axis at various  $z$  positions relative to the top of the sample ( $z = 10, 35, 65\text{mm}$ ).

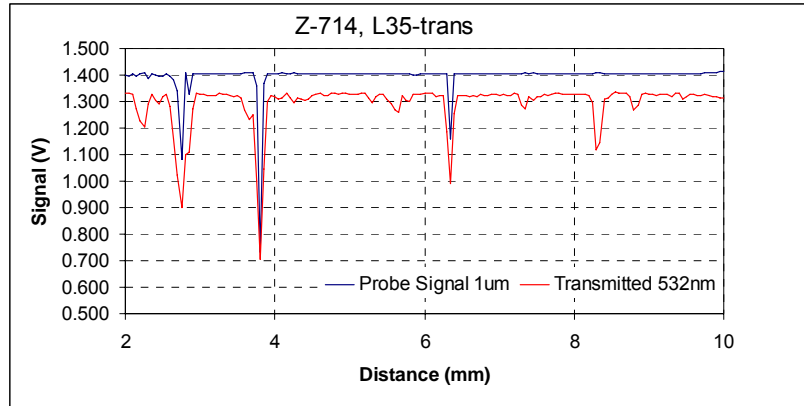


**Fig. 26** Details of the scan of sample Z-714 along the X-axis at position  $z = 35\text{mm}$

### Light Scattering Tomography

Laser scattering tomography (LST) reveals microscopic and submicroscopic particles by elastic scattering of light, in a similar manner that of the old method of ultra-microscopy. Moriya and Ogawa who introduced focused laser radiation and applied this method to characterize a variety of materials<sup>1</sup>. Our LST setup uses an intense laser beam with a wavelength in the transparent region of the material under investigation. The beam is focused on the region of interest inside the sample. The illuminated region is imaged at  $90^\circ$  by a microscope, and the distribution of scatters is determined after data processing.

Figure 27 shows our experimental setup. The beam of a He-Ne laser is shaped by a telescope. The light irradiates the scatterers inside the sample, and it is possible to observe 2D LST images. A microscope images the irradiated scatterers onto a CCD camera. The microscope has a low numerical aperture ( $\text{NA}=0.08$ ). This low N.A. restricts the resolution to about  $10\text{ }\mu\text{m}$ . An image processing system is used for frame grabbing and digital integration of the video images. The image processing is then performed by computer. Prior to the beginning of this program, we had added a vertical and horizontal translation stage covering a  $20\text{ mm}$ -range with a precision of  $0.1\text{ }\mu\text{m}$  as well as a  $360^\circ$  rotation stage with an angular precision of  $0.1^\circ$ . The rotation stage enabled us to observe the shape and the symmetry of scattering defects more clearly. We also implemented LabView VI to control these stages, perform the image capture and process the 2-D images.

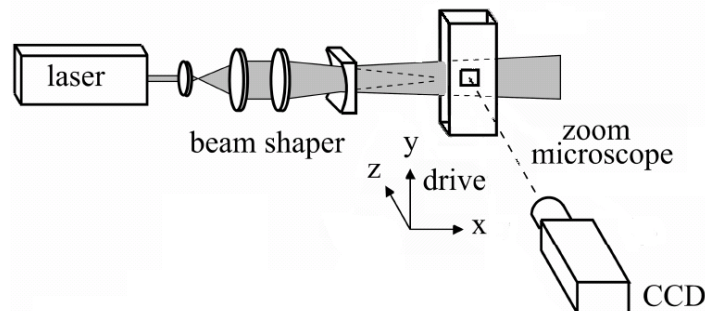


**Fig.27** Details of light scattering tomography

<sup>1</sup> K. Morea and T. Ogawa, "Observation of growth defects in synthetic quartz crystals by light-scattering tomography " J. Crystal Growth, Volume 44, Issue 1, August 1978, Pages 53-60

LST gives images with high contrast, which can resolve the faintest objects. The defects are observed inside the bulk without damaging the sample. LST is a well-established technique for studies of inclusions (pores or precipitates) and defects decorated by inclusions (such as dislocations). The detectability of defects by this system is dependent upon their scattering power, which depends on the defect's physical characteristics such as refractive index difference, piezo-optical birefringence around dislocations and their shapes. The resolving power of this system is better than that of an objective lens because light scattering is caused by much smaller particles and/or refractive index irregularities than the resolving power of the lens, which is very similar to seeing smoke though not being able to image individual particles in the smoke with our eyes. It is a somewhat novel application to adapt LST to measure the size and density of scatters in ceramics. The typical methods for scattering measurement are either measuring scattering loss coefficient over certain length, or using SEM and SAM to identify scatters at the nanoscale. The advantage of LST for ceramic scattering measurement is to provide a bulk view from  $\mu\text{m}$  to  $\text{mm}$  size, as well as more accurate statistical data of scatters' size, density and distribution.

The following pictures (Figs. 28 and 29) show a comparison between the LST images obtained in the five YAG samples studied, all acquisition parameters being equal. The nature of the scattering centers has yet to be fully determined. Each LST image shown here was compiled from 50 horizontal translational images, with a step size of  $10\ \mu\text{m}$ .

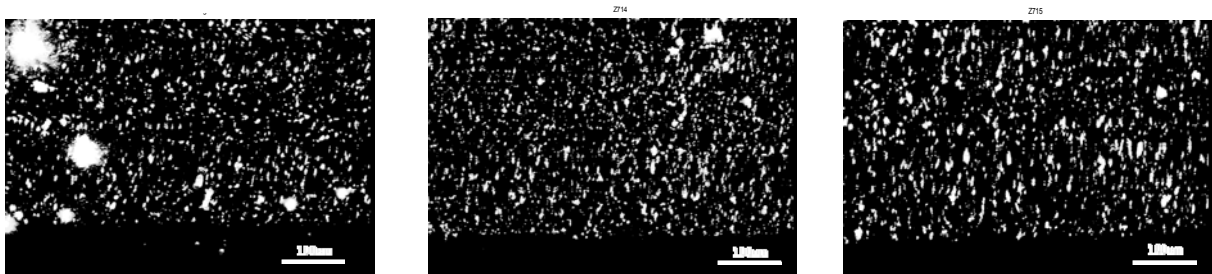


**Fig. 28** Comparison of the density of scatters seen by light scattering tomography in sample Z-713 (YAG, left), Z-714 (Nd:YAG, center) and Z-715 (Gd:YAG, right).

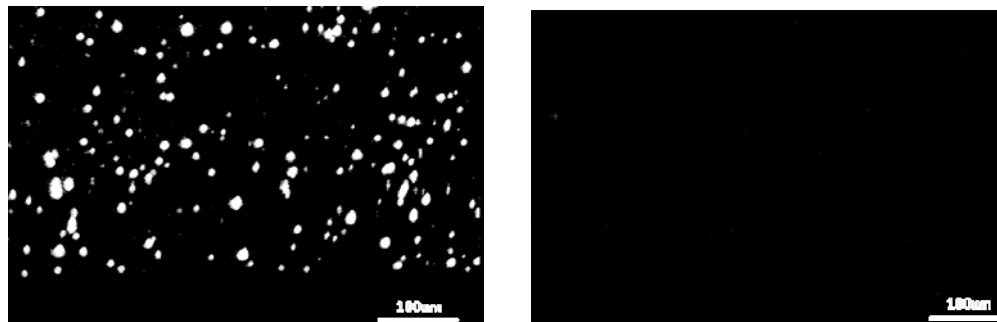


**Fig. 29** A comparison of the density of scatters seen by light scattering tomography in a Nd:YAG ceramic sample from Konoshima (Konol, left) and single-crystal of Nd:YAG (Sc1, right) (The same image acquisition parameters were used as for the images shown in Fig. 28.)

From these pictures, we were able to estimate the density and the size of the scatters (Table 3). To confirm the results of LST measurement, the transmittance spectra of Z713 was measured and the Mie model in section 2.2 was used to fit the spectra. The fitting size of scatters was  $0.34\mu\text{m}$  and the number of density was  $1.75 \times 10^5 \text{ cm}^{-3}$ , which validated our estimate from LST.

**Table 3:** Density and size of scatters in the samples investigated by LST

Sample	Z713	Z714	Z715	Kono1	Sc1
Scatter density ( $\text{cm}^{-3}$ )	$8 \cdot 10^4$	$1.1 \cdot 10^5$	$1.04 \cdot 10^5$	$1.5 \cdot 10^3$	Below detection limit
Scatter size ( $\mu\text{m}$ )	$< 1$	$< 1$	$< 1$	2~10	Below detection limit

Samples Z-713, Z-714 and Z-715, all made by the reactive sintering method, seemed to have on average 10 times smaller scatter sizes than in sample Kono1 made by the non-reactive sintering method. However, the former presented up to 100 times more scattering centers than the latter. Results obtained by both LST and thermalized absorption techniques suggested that scattering occurred predominantly from micro-porosity.

For a continuation of this work, we planned to use different laser sources at various wavelengths to better characterize the nature and the size of scatters as well as perform better depth integration and 3-D image processing. Due to the move of the ceramics component to UCF, this work has been delayed.

### Laser Properties

The laser performance of the Nd:YAG sample Z-714 was tested in a simple planar-concave cavity. The sample was pumped at 808 nm by a laser diode, the optics were HR coated at 1064 nm and the end-mirror had a 20 cm radius of curvature (Fig. 30). An anti-reflection coated, 1 at% Nd:YAG single-crystal was also tested under the same conditions for the sake of comparison. The laser performance is plotted in Figs. 31 and 32.

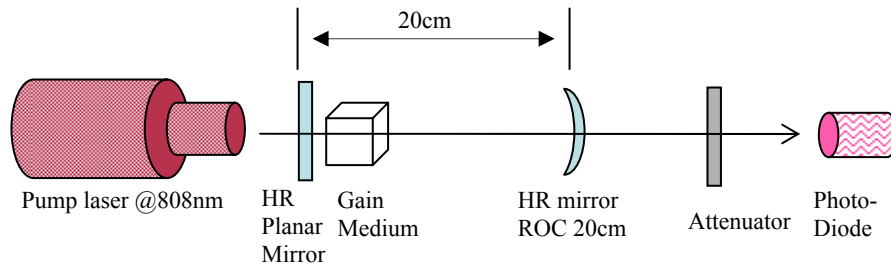


**Fig. 30** Schematic of the laser set-up with a planar-concave cavity

The laser threshold for both ceramic and single-crystal was 5.2 W. The optical-optical efficiency of the uncoated ceramic was 9.8 % versus 14.9 % for the AR-coated single-crystal.

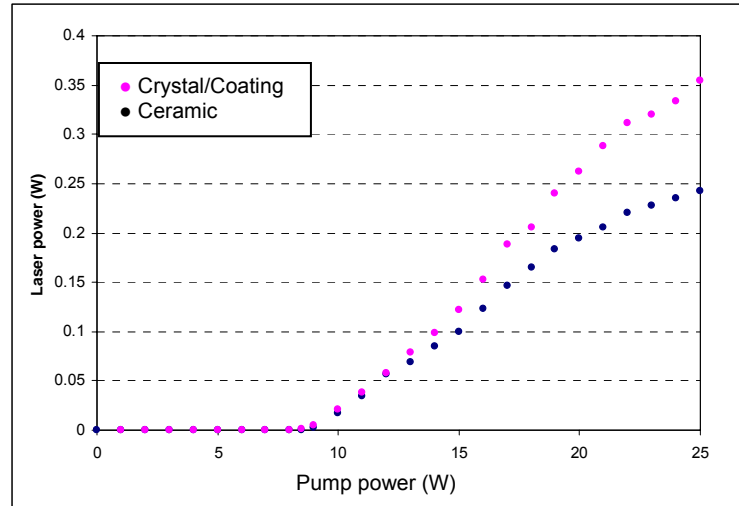


**Fig. 31** Laser performance of both Z-714 ceramic and Nd:YAG single crystal Sc1.

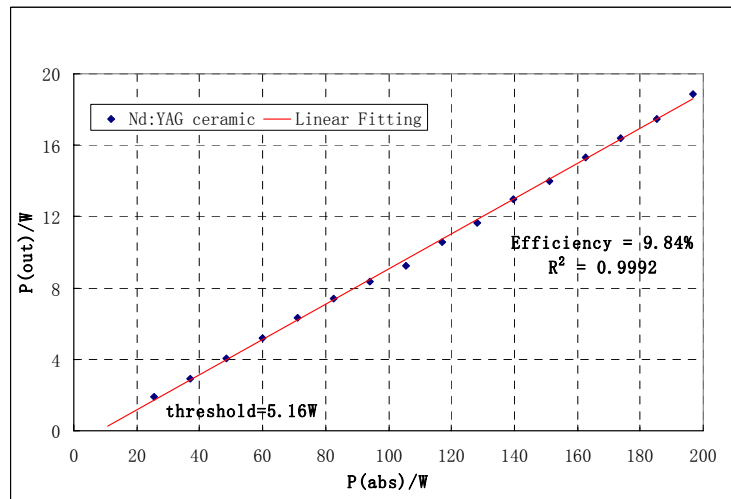


**Fig. 32** Calibrated laser efficiency of sample Z-714

### Directions for Continuing Research on Ceramic Laser Host Materials

The achievement of stable processing conditions and the acquisition of supplemental equipment in our ceramic lab (spray-dryer), helped us to control the agglomeration state of the starting powders and make us confident that the optical quality of the ceramics we produce will continue to improve. This allowed us to study further the diffusion of dopants and improve the fabrication techniques for laser ceramic composites.

The research described here was also successful in developing the tools necessary to quantify optical losses in ceramic laser host materials. We showed a significant correlation between processing variables and optical quality in ceramic materials. Our main goal in future research

efforts will be to understand these trends and exploit them to further lower optical losses in ceramic laser host materials. Many questions remain to be answered when the fabrication and characterization work has been re-established at the University of Central Florida, and it will have crucial consequences as far as the fabrication of engineered ceramic gain media is concerned.

## II. Development of Tm-Doped Fiber Lasers and Fiber Laser Amplifiers

### Mode-Locked Thulium-Doped Fiber Lasers

Thulium-doped lasers have a wide gain spectrum ranging from  $\sim 1.8$  to  $2.1 \mu\text{m}$ , depending on the host material. A pulsed source with this wide range of wavelengths has many uses, including dielectric laser-driven particle-acceleration [1], mid-IR generation for spectroscopy through either down-conversion [2] or super-continuum generation [3], and eye-safer applications, such as remote sensing [4]. The broad gain spectrum makes  $\text{Tm}^{3+}$  an excellent candidate for generating extremely short mode-locked pulses that would satisfy the ultrafast operation requirement for the aforementioned applications.

Tm-doped fiber lasers have previously been mode-locked using saturable absorbers, such as carbon nanotubes [5-7] and semiconductor saturable absorbing mirrors (SESAMs) [8], as well as artificial saturable absorbers, such as nonlinear polarization rotation [9] and a combination of SESAM and a NALM [10, 11]. By utilizing an optical fiber to produce these mode-locked lasers, the many advantages of fiber lasers can be exploited. Fiber lasers provide the ability to produce long cavity lengths in a compact form. With an all-fiber configuration, there is no need for frequent alignment, unlike as is often the case with free-space solid-state lasers. These benefits can help reduce the lasers susceptibility to external noise sources [12].

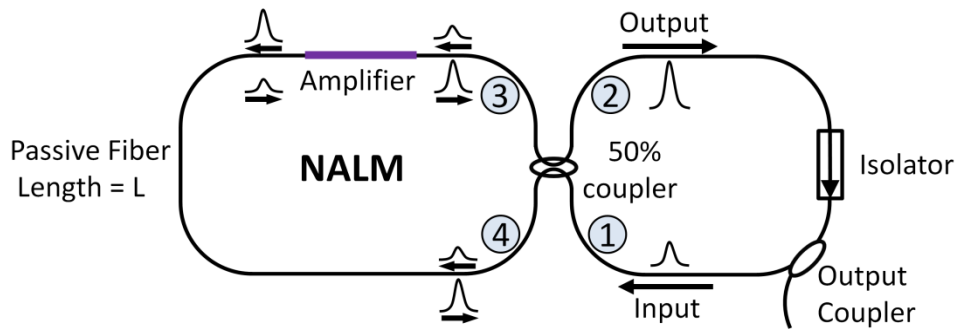


**Fig. 33.** Schematic of an F8L with a NALM. The left loop is a NALM, while the right loop contains an isolator that limits propagation to one direction. The NALM acts in conjunction with the isolator to create a nonlinear fiber-based saturable absorber that prefers pulse operation.

### Figure-Eight Laser (F8L)

The first all-fiber mode-locked laser configuration reported in the literature was the figure-eight laser (F8L) [13, 14], using an Er-doped fiber as the gain fiber. An F8L makes use of a fiber-based saturable absorber based on the Kerr effect. This saturable absorber is easy to implement in an all-fiber configuration.

### Mode-Locking Mechanism

The saturable absorption effect in an F8L is created by a nonlinear amplifying loop mirror (NALM) [15] in conjunction with a fiber isolator. In an F8L, the NALM, which consists of an amplifier placed asymmetrically in a loop of passive fiber, is coupled to a second loop containing



the isolator and output coupler with a 2x2 50% coupler, as shown in Fig. 33. The isolator determines the direction of propagation for the pulse traveling in the second loop. The isolator causes the pulse in the right-side loop to enter port 1 of the central coupler. The pulse is then split equally into ports 3 and 4. The pulse exiting through port 3 enters the amplifier and is amplified before propagating through the passive fiber length whereas the pulse exiting port 4 propagates through the passive fiber before being amplified. The difference in peak intensity causes the pulses counter-propagating through the NALM to accumulate differential nonlinear phase shifts  $\Delta\phi_{34}$  due to self-phase modulation (SPM). When these pulses recombine at the central coupler, this phase difference causes the pulses to interfere destructively in port 1 and constructively in port 2, and therefore be transmitted through port 2, with a transmission coefficient

$$T = Ge^{-\alpha L} (1 - 2\kappa(1 - \kappa) \{1 + \cos(\Delta\phi_{34})\}), \quad (1)$$

where  $G$  is the gain of the amplifier,  $\alpha$  is the loss of the passive fiber, and  $\kappa$  is the power coupling ratio of the central coupler [15]. The nonlinear phase difference is

$$|\Delta\phi_{34}| = (1 - \kappa - \kappa G) P \gamma L_{eff}, \quad (2)$$

where  $P$  is the instantaneous power of the pulse entering the NALM,  $\gamma$  is the nonlinear coefficient of the passive fiber, and the effective length of the passive fiber is

$$L_{eff} = \frac{1 - e^{-\alpha L}}{\alpha}. \quad (3)$$

Oscillation is possible only for high peak powers, as is the case in pulsed operation. This discrimination for high-peak-power operation is equivalent to a saturable absorption effect. The peak power of the pulse in the F8L cavity must be equal to the peak power of a soliton pulse,

$$P_{pk,NALM} = \frac{3.104 |\beta_2|}{\gamma \tau^2}, \quad (4)$$

where  $\beta_2$  is the second order dispersion and  $\tau$  is the pulse width [13].

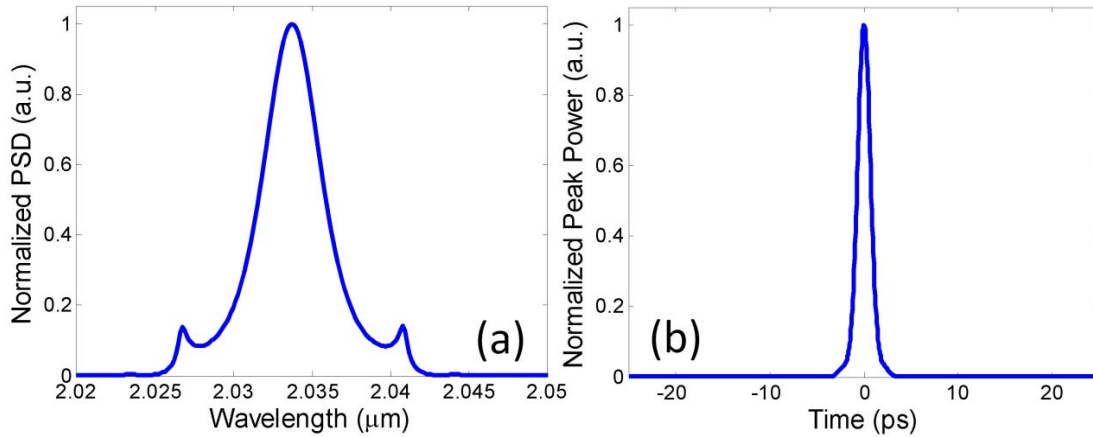


**Fig. 34.** Simulation of the experimental all-fiber Tm-doped F8L (see text for parameter values). (a) Simulated output spectrum had a 3-dB bandwidth of approximately 4 nm. Kelly sidebands. (b) Simulated temporal output of the F8L is shown. The pulse width is approximately 1.6 ps.

### Simulations of a Tm-doped F8L

The experimental work is based on the Tm-doped all-fiber F8L configuration. To model the pulse formation and propagation in a Tm-doped F8L with a NALM, several approximations had to be made. Following [16], the gain spectrum of the Tm-doped amplifier section in the NALM

was approximated by a Lorentzian. Gain saturation was assumed to be exponential. To propagate the signal around the experimental cavity, the nonlinear Schrödinger equation (NLSE) was used. The split-step Fourier (SSF) method was implemented to solve the NLSE [17]. This method can be performed numerically by implementing the fast Fourier transform (FFT).

A model of a Tm-doped all-fiber mode-locked F8L was created with parameters similar to the experimental F8L. The  $\beta_2$  of the fiber in the cavity was  $-100 \text{ fs}^2$ , while the  $\beta_3$  was assumed to be zero. The nonlinearity provided by the passive fiber was  $\sim 0.4 \text{ W-km}^{-1}$ . The central coupler had a 50% coupling ratio and the output coupler had a 10% coupling ratio. The amplifier was assumed to have an estimated 35-dB small-signal gain and a saturation energy (which sets whether or not the laser operates with low or high pulse energy [16]) of 60 pJ from a length of 8 m of gain fiber. The estimated gain bandwidth from the amplified spontaneous emission spectrum was 50-nm bandwidth around a center wavelength of 2034 nm. The passive fiber in the NALM was assumed to be 7 m in length, while the passive fiber in the output coupling loop was 5 m. After about 200 round trips, the soliton pulse had grown from the seeded random noise to a stable pulse with the spectral and temporal output plotted in Fig. 34 (a) and (b), respectively. The simulated soliton pulse had a spectral bandwidth of about 4 nm and pulse width of approximately 1.6 ps with 50 pJ of pulse energy.

#### Mode-Locked Thulium-Doped All-Fiber F8L

We designed, assembled, and tested an all-fiber mode-locked laser in the F8L configuration [18]. The experimental oscillator is shown in Fig. 35. The loop on the left is a NALM [15], which acts as an artificial fiber-based saturable absorber in conjunction with the isolator. The F8L configuration prefers pulsed operation over continuous-wave (CW) operation [13].

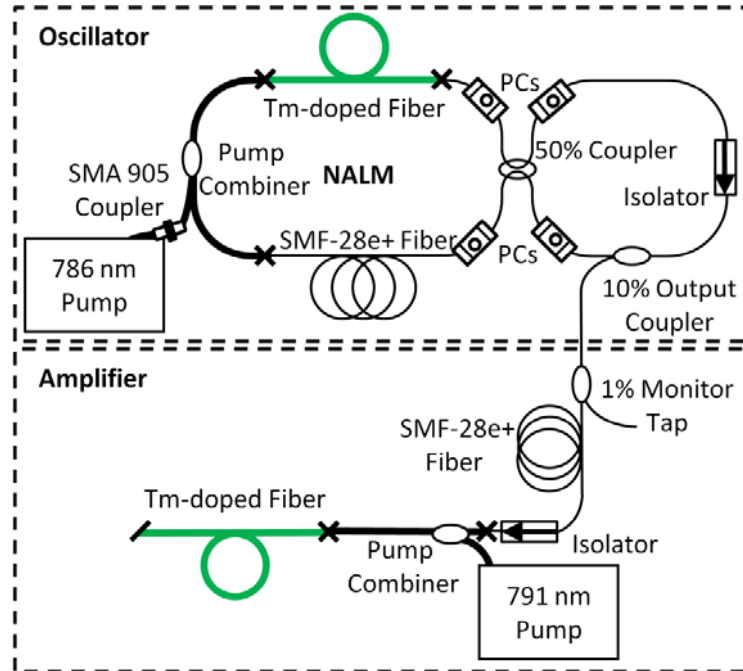


**Fig. 35.** Diagram of the mode-locked all-fiber oscillator and amplifier. X denotes a splice between dissimilar fibers. The NALM comprised 8 m of Tm-doped fiber and 7 m of SMF-28e+ fiber. The second loop was 3 m in length for an overall cavity length of 20 m. A 13-m length of SMF-28e+ pre-chirped the pulse entering the amplifier with anomalous GVD. The end of the 11-m Tm-doped fiber amplifier was angle-cleaved to reduce the reflection.

Fiber components in the 2- $\mu\text{m}$  wavelength range are still either unavailable commercially or exhibit modest performance, which limited our options during this work. A previous version of the F8L [19] used mainly C-band components, because 2- $\mu\text{m}$  components were largely unavailable. Most of these components have been replaced since then by 2- $\mu\text{m}$  components; however, these new components have more loss than the C-band components at their respective operating wavelength range. Reported here are the results of the F8L constructed using the 2- $\mu\text{m}$  components. The performance of Tm-doped fiber lasers will only improve as 2- $\mu\text{m}$  components are further developed and their performance progresses.

The left loop of the F8L in Fig. 35 consisted of 7 m of SMF-28e+ fiber, 8 m of Nufern double-clad Tm-doped fiber with a 10- $\mu\text{m}$  diameter core doped with 5 wt.% of  $\text{Tm}^{3+}$  and a 130- $\mu\text{m}$  octagonal-cladding diameter, and assorted leads of SMF-28 fiber from the fiber components. SMF-28e+ fiber was chosen as the passive fiber because its measured loss at 2  $\mu\text{m}$  is relatively low, namely around 10 dB/km, compared to more than 100 dB/km for the SMF-28 fiber. The gain fiber was cladding-pumped with an SMA 905 connectorized Dilas fiber-coupled laser diode at 786 nm through a (2+1)x1 pump combiner. The maximum usable pump power was limited to 9 W by the power rating of the pump combiner. The maximum pump power absorbed by the Tm-doped fiber was estimated to be 3 W. The second loop, 3 m in length, consists of a 2- $\mu\text{m}$  fiber-coupled isolator and a 10% fiber output coupler. The isolator had an insertion loss of 0.65 dB and an extinction ratio of 37 dB at 2  $\mu\text{m}$ . A 50% 2x2 fused fiber coupler joined the two loops together. The 2x2 central coupler had an insertion loss of 0.8 dB, and its coupling ratio covered a range of around  $50\% \pm 2\%$  over an 80-nm bandwidth centered at 2020 nm. The combined cavity length was  $\sim 20$  m. A polarization controller (PC) was inserted on each lead of the central coupler to ensure that the counter-propagating pulses interfered with maximum contrast.

The approximate round-trip loss of the F8L was 4 dB. Most of this loss originated from the passive fiber loss in the components made from SMF-28 fiber and from the insertion loss of these components, especially the isolator and central coupler. Also, the splices between the Tm-doped gain fiber and the passive fiber had a loss of 0.15 dB per splice, due to the difficulty of aligning an octagonal-clad fiber. As components in this wavelength range mature, the losses will decrease and the laser performance will improve markedly.

As the launched pump power was varied, as shown in Fig. 36, the F8L operated in several regimes. The oscillator initially operated as a CW laser. At  $\sim 4$  W of pump power, CW oscillation became unstable and mode-locking self-started, generating pulses at a repetition rate  $f_{rep} = 10.4$  MHz with an average power  $P_{avg} = 0.66$  mW. This corresponds to an output pulse energy of 60 pJ for the Tm-doped F8L. As the pump power increased,

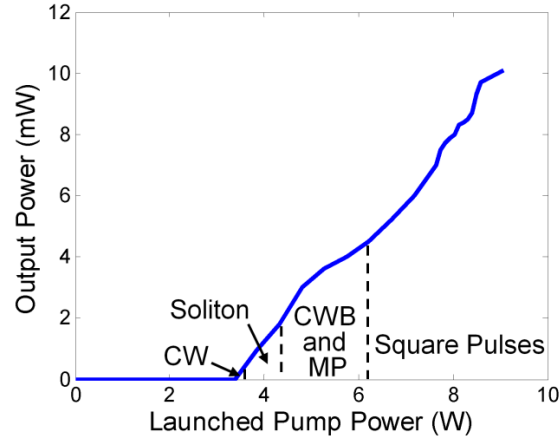


**Fig. 36.** Oscillator output power versus launched pump power. At low pump power the F8L initially oscillates as a CW laser. As the launched pump power is increased, the F8L mode-locks and generates soliton pulses. At still higher pump power, the soliton pulses begin to experience CW breakthrough (CWB) and multi-pulsing (MP). At ~6W of launched pump power, square pulses form.

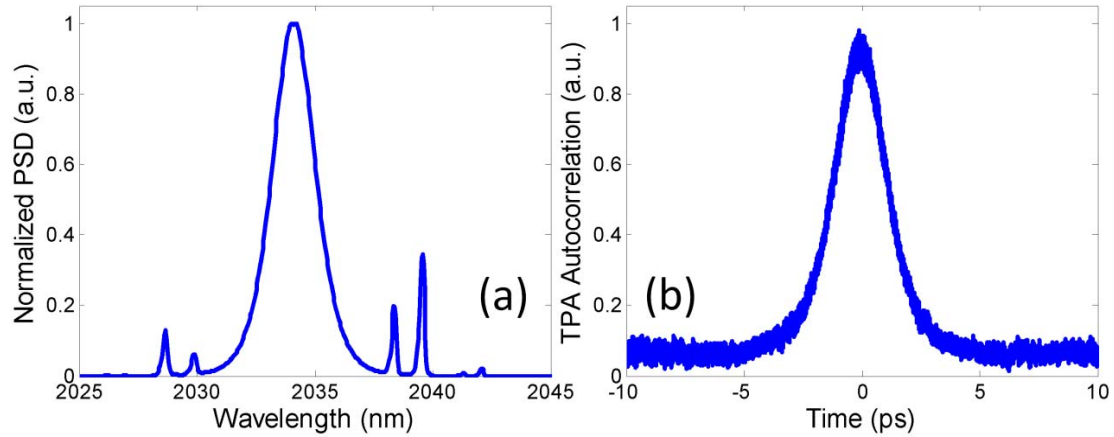


**Fig. 37.** Measured normalized oscillator power spectral density (PSD) and intensity autocorrelation for the soliton pulse regime. (a) The spectrum is centered around 2034 nm with a spectral bandwidth of 3 nm. (b) An autocorrelation measurement using two-photon absorption in a silicon detector. The full-width half maximum of the measured trace is 2.3 ps, which corresponds to a pulse width of 1.5 ps.

Figure 37(a) shows the output spectrum of the soliton pulses, measured with a Yokogawa AQ6375 optical spectrum analyzer. The spectrum in the figure had a bandwidth of about 3 nm. An intensity autocorrelation trace of the soliton pulses (Fig. 37(b)) was measured using two-photon absorption (TPA) in a Si photodiode. The measured autocorrelation trace width was 2.3 ps, which corresponds to a 1.5-ps pulse width. Using the pulse width, 1.5 ps, and the spectral bandwidth, 3 nm, the time-bandwidth product was calculated to be 0.33, which is nearly transform-limited. There was no dispersion compensation within the oscillator, which caused the spectral bandwidth of the oscillator to be limited by dispersion. The peak power of the output pulse was only 35 W due to the 10% output coupler. The peak power of the pulse traveling in the cavity was approximately 350 W, which closely matched the calculated switching power of the NALM from Eq. 4 (~325 W).

The simulated output pulse characteristics, 50-pJ pulse energy, 1.6-ps pulse width and 4-nm spectral bandwidth (see Fig. 34), were very close to the measured experimental values, 60-pJ

pulse energy, 1.5-ps pulse width and 3-nm spectral bandwidth. The differences in pulse width and spectral bandwidth most likely arise from the simplifications used in the model (i.e., the effects of birefringence and third-order dispersion were ignored for this simulation) and the unknown properties of the fibers in the 2- $\mu\text{m}$  wavelength range.

The slope efficiency of the oscillator with respect to launched pump power is 0.2% (see Fig. 36). This low value was partially caused by poor coupling of the 786-nm fiber coupled diode pump into the pump combiner due to the use of an SMA 905 coupler with 100- $\mu\text{m}$  core diameter fibers, causing  $\sim 1.25$  dB of loss. As a result of the mismatch between the first cladding average diameters of the pump combiner (150  $\mu\text{m}$ ) and of the gain fiber (130  $\mu\text{m}$ ), the pumps experienced 0.5 dB of insertion loss in the pump combiner, as well as 0.15 dB of splice loss. In total, the 786-nm pump diode experienced  $\sim 1.9$  dB of loss before entering the gain fiber. A second cause of the low slope efficiency was amplified spontaneous emission (ASE). Upon opening the cavity around the isolator, a large amount of ASE ( $\sim 1$  W at 8 W of pump power) was found in the direction to be blocked by the isolator (see Fig. 36). This large amount of ASE, if present during oscillation, was not detectable through the output coupler, because it would have been blocked by the isolator. In addition, high cavity loss, mainly from the 2- $\mu\text{m}$  components, also reduces the efficiency. Again, this performance will only improve as the diversity and characteristics of commercial 2- $\mu\text{m}$  fiber components progress in the future.

Strong Kelly sidebands, which come from periodic spectral interference between the soliton wave and a co-propagating dispersive wave, were predicted in the theoretical output spectrum (see Fig. 34(a)) and observed in the experimental output spectrum (see Fig. 37(a)). This is also a sign that the pulses were close to transform-limited [20]. The Kelly sidebands contained 5% of the pulse energy.

The stability of the soliton operation strongly depended on, and was quite sensitive to, the position of the PCs. CW breakthrough would often occur (beginning with the Kelly sideband peaks) if the PCs were slightly shifted from their optimum positions for soliton operation. Since the central coupler had a coupling ratio that deviated from 50%, a CW path through the cavity existed. The PCs allowed for use of the coupler's polarization dependent loss (PDL) to compensate for this deviation from 50%, thus blocking the CW path. This partially explains the extreme sensitivity to PC positioning as well as the need to replace the 65% 2x2 coupler used in an earlier prototype [19].

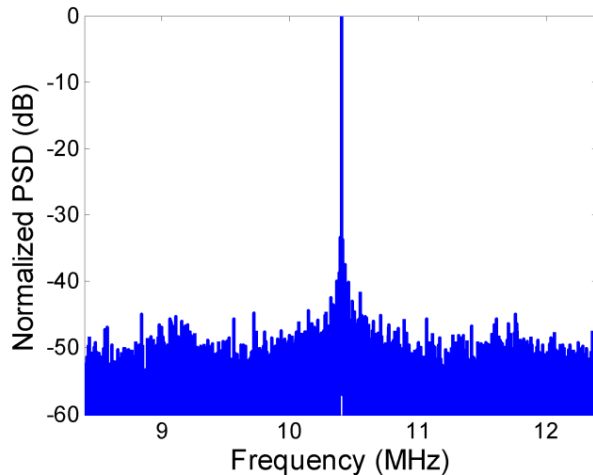


**Fig. 38.** Measured RF spectrum of the oscillator for the soliton pulse regime, with a 300-Hz resolution bandwidth. The center frequency of the RF spectrum, 10.4 MHz, is the pulse repetition rate. The amplitude noise of the pulse can be estimated from the spectral width of the RF spectrum.

The RF spectrum of the pulse train, shown in Fig. 38, was measured using a 10-GHz extended InGaAs photodiode and a 40-GHz RF spectrum analyzer with a 300-Hz resolution bandwidth. The RF spectrum of the fundamental harmonic can be used to compute the amplitude noise in the mode-locked laser. From the measured RF spectrum [21], the amplitude noise was calculated to be 1.1% in the soliton mode-locking operation region. Fabricating an all polarization-maintaining fiber F8L would increase the stability of the laser as well as reduce the effects of environmental fluctuations. To further increase the stability, the gain fiber can be core-pumped by a stable 1.5- $\mu\text{m}$  diode laser in combination with an erbium-doped fiber amplifier.

As the pump power increased, CW breakthrough and then multi-pulsing were observed (see Fig. 36). A type of multi-pulsing referred to as harmonic mode-locking, where the multiple pulses generated are temporally evenly separated [22], was also observed in the Tm-doped F8L, with repetition rates higher than 100 MHz.

At  $\sim 6$  W, the F8L transitions to a new mode of operation where soliton pulses are no longer produced. As the peak power of the pulse reached the peak power allowed for maximum transmission through the NALM, the peak power was clamped, and any further increase in gain produced a temporal and spectral broadening of the pulse [23]. This generated stable square-shaped pulses at a 10.4-MHz repetition rate with pulse widths from  $\sim 100$  ps to 20 ns and between 15 nm to 25 nm of corresponding spectral bandwidth. An example of the spectral and temporal characteristics of these pulses can be seen in Fig. 39 (a) and (b), respectively, which shows a square pulse with a bandwidth of 20 nm and a pulse width of 1 ns. Square-shaped pulses from this regime may be useful for remote sensing (e.g., spectrally sensitive LIDAR [24]) and machining applications [25].

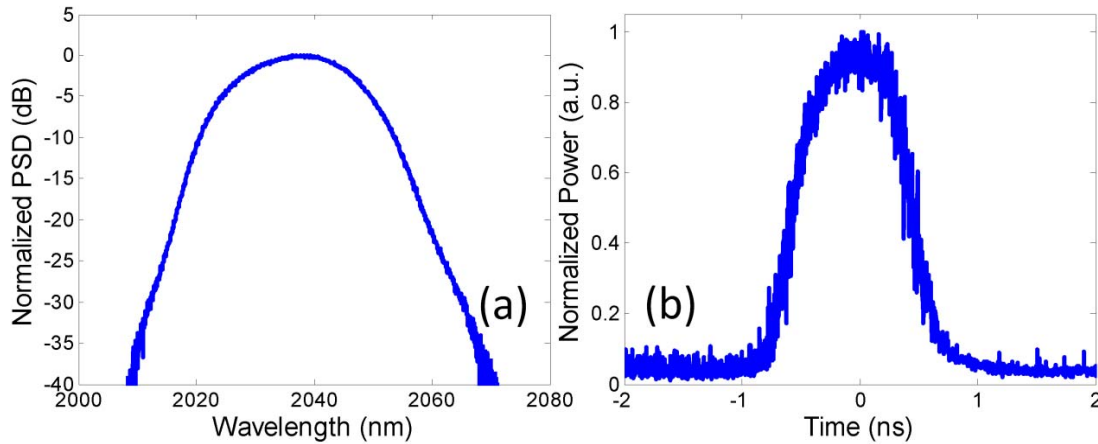


**Fig. 39.** (a) Normalized PSD and (b) temporal profile of the oscillator's square pulse regime. Tuning of the pulse width (100 ps to 20 ns) and spectral width (15 nm to 25 nm) can be achieved by varying the pump power as well as the PCs. The spectral width shown in (a) is 20 nm, while the pulse width in (b) is 1 ns.

#### Amplification of Mode-locked Lasers in Thulium-doped Fiber

**Chirped Pulse Amplification** - To generate the peak powers required for the aforementioned applications, the nonlinear effects in the fiber that can cause pulse distortion must be avoided. Severe pulse distortion begins to occur once the phase shift due to self-phase modulation (SPM) is larger than  $2\pi$ . This limits the output peak power of an amplifier to

$$P_{pk,max} = \frac{2\pi}{\gamma L_{eff}}, \quad (5)$$

where  $\gamma$  is the nonlinear coefficient, which is inversely proportional to the effective area  $A_{eff}$ , and the effective length is

$$L_{eff} = \frac{1 - e^{-gL}}{g}, \quad (6)$$

with  $g$  as the gain coefficient of the amplifier and  $L$  as the physical length of the amplifier [26].

Chirped pulse amplification reduces the effective nonlinearity experienced in the amplifier by prechirping and temporally broadening the pulse (thus reducing the peak power). After amplification, the pulse can be recompressed. The development of chirped pulse amplification (CPA) in thulium-doped fibers is still lagging well behind the 1- $\mu$ m fiber CPA systems. Currently, pulsed Tm-doped fiber laser systems operate at similar average powers, either concentrating on systems with low repetition rate (100 kHz) and high pulse energy (150  $\mu$ J) [27], high repetition rate (500 MHz) and low pulse energy (5 nJ) [28], or somewhere in between with respect to both measures (e.g., 37 MHz and 150 nJ in [29]). Average power scaling of amplified sub-picosecond Tm-doped fiber lasers has only recently reached 10 W [27] and is typically around 1 W. However, none of these systems are completely in an all-fiber form, from the oscillator to the amplifier.

Since the desired final pulse energy and peak power of the Tm-doped all-fiber mode-locked master-oscillator power amplifier (MOPA) were low (average powers of  $\sim 1$  W), compression could be performed within the amplifier's gain fiber without experiencing damage or detrimental amounts of nonlinearity. This provided an all-fiber amplifier configuration to accompany the all-fiber oscillator. Compression of the stretched pulse within the gain fiber occurs due to nonlinear pulse compression. Nonlinear pulse compression uses the SPM that the amplified pulse experiences to provide large amounts of an approximately linear up-chirp (analogous to normal GVD) [30]. This can even be done in a gain fiber that would normally have anomalous GVD. By using the amplifier's gain fiber as the compressor, the pulse stretcher must have anomalous GVD (or provide a linear down-chirp). The pulse stretcher chosen in the experimental configuration was a passive fiber that provided anomalous GVD in the 2- $\mu$ m range. Due to the relatively low pulse energy and peak power required for the desired initial applications of this Tm-doped all-fiber MOPA, only a slight stretch of the soliton pulse from the oscillator was required to prevent severe pulse distortion from excessive nonlinearity. Stretching of the pulse was performed by a reasonable length of passive fiber.

**Simulations of Experimental Thulium-Doped Amplifier** - The amplifier configuration used in the experiment was simulated using the same split-step Fourier method, with the addition of shock formation to the nonlinear operator. The same parameters given for the gain and passive fibers from the oscillator were used. Beginning with an unchirped hyperbolic secant pulse from the oscillator, the pulse propagates first through 13 m of SMF-28e+ (the passive fiber stretcher) and then 11 m of single-mode Tm-doped gain fiber. The temporal evolution of the pulse is shown in Fig. 40(a). As the peak power of the pulse is greatly enhanced at the end of the amplifier (due to the  $\sim 25$  dB of gain and the temporal compression provided by the amplifier), the pulse in Fig. 40(a) is only visible at the very end of the amplifier. By normalizing the peak power of the pulse to the maximum peak power at every length, as seen in Fig. 40(b), the



temporal behavior of the pulse can be observed. The pulse initially stretches, then compresses as the pulse energy increases. The entirety of the pulse compression occurs within the last short segment of the amplifier, because this is where the pulse energy and corresponding peak power are large enough (as seen in Fig. 40(a)) to create enough SPM to compensate for the previously accumulated down-chirp in the anomalous GVD passive fiber and initial segment of the gain fiber.

This behavior is further illustrated in Fig. 41(a), which displays the spectral evolution of the pulse as it propagates through the pre-chirp fiber and the amplifier gain fiber. Again, the pulse spectrum can only be seen near the end of the amplifier segment, because this is where the peak power is highest. Figure 41(b) shows the spectrum normalized to the maximum power spectral density at every length, which reveals that there is no modification of the pulse spectrum through the passive fiber and the initial portion of the gain fiber. In this region, dispersion is the dominant effect, which does not affect the spectrum of a propagating pulse. The spectral broadening and modulation due to SPM only appear at the very end of the amplifier, because this is the only region where the peak power of the pulse is high enough to affect the spectrum.

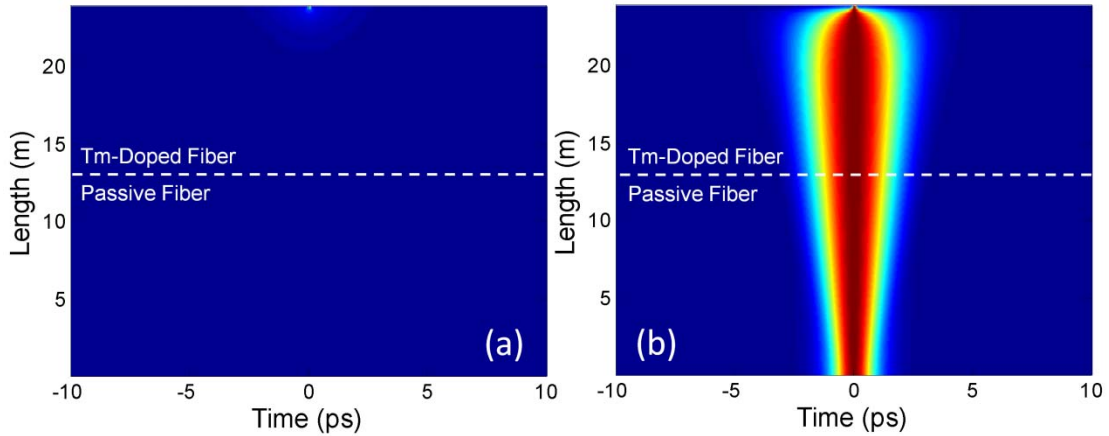


**Fig. 40.** Temporal pulse propagation in pre-chirp fiber and amplifier's gain fiber. (a) Simulated temporal pulse propagation along the pre-chirp fiber and the amplifier's gain fiber. Since the pulse peak power increases drastically at the very end of the amplifier, the pulse is only observable at the end of the amplifier segment. (b) Same as (a), but the peak power is now normalized to the peak power at every location along the fibers to show the evolution of the pulse shape. The pulse broadens through the passive fiber and much of the amplifier. At the end of the amplifier, the peak power is finally large enough to induce enough SPM to compensate for the accumulated chirp and compress the pulse.



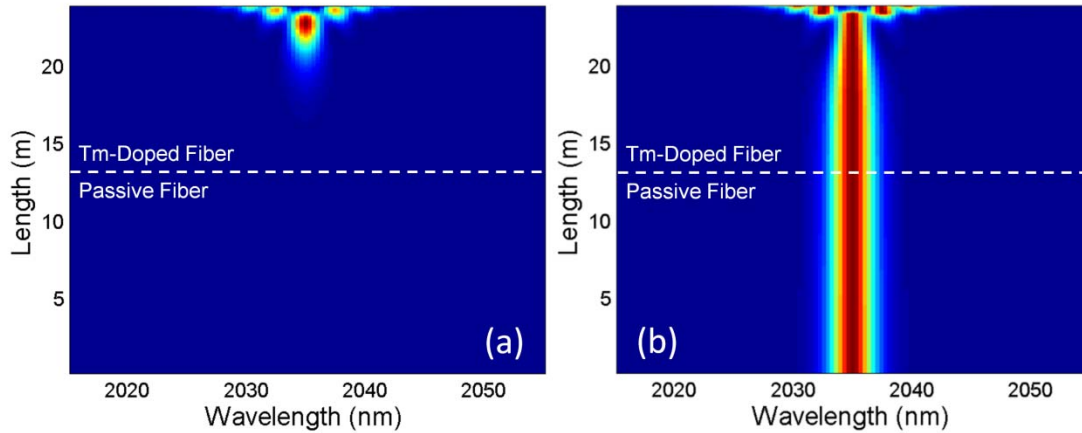


**Fig. 41.** Spectral evolution along pre-chirp fiber and amplifier's gain fiber. (a) The simulated spectral evolution through the pre-chirp and amplifier fiber is shown. Again, the peak power of the pulse is much higher at the end of the amplifier, which causes the pulse to be observable just at the end of the amplifier segment. (b) After normalizing to the peak power at every location along the fiber length, the evolution of the spectrum is observable. The spectrum remains unchanged for much of the propagation through the passive fiber and most of the amplifier. At the end of the amplifier, the peak power is finally large enough to create enough SPM to modulate of the spectrum.

Experimental Amplified Thulium-Doped F8L - The output of the F8L oscillator was passed through a 1% output coupler used to monitor the output of the oscillator before propagating to the amplifier, as shown in Fig. 35 [18]. The 13-m SMF-28e+ pulse stretcher provided the necessary anomalous GVD to stretch the pulse by a factor of two—from 1.5 ps to ~3 ps. An isolator with a 0.75-dB insertion loss and 37-dB of isolation was placed at the end of the stretcher to protect the oscillator from any emission from the amplifier in the backward direction (either ASE or reflections). The amplifier stage consisted of an 11-m length of the same double-clad gain fiber used in the oscillator, with a 10- $\mu\text{m}$  Tm-doped core and a 130- $\mu\text{m}$  octagonal first cladding, pumped with up to 7 W from a 791-nm Dilas fiber-coupled laser diode through a (2+1)x1 pump combiner. This provided more than 25 dB of gain. The end of the gain fiber was angle-cleaved at approximately  $8^\circ$  to reduce the reflection back into the amplifier.

Experimental Results and Discussion - Figure 42 shows the measured output power of the amplified soliton pulses from the F8L for increasing launched pump power. The maximum slope efficiency of the amplifier was 22.7% after the pulses were amplified to energies that saturated the gain of the amplifier. At the output of the oscillator, the soliton pulses had a width of 1.5 ps, 60 pJ of energy, and a 3-nm spectral bandwidth. Spectral broadening and consequent temporal compression through SPM in the amplifier [30] allowed for the slightly pre-chirped pulses to be compressed to 370 fs at the maximum average output power of 710 mW. The down-chirp created by the anomalous-dispersion fiber before the amplifier was compensated by the up-chirp produced by SPM. Figure 43(a) shows the output spectrum at the maximum pump power. The output-pulse bandwidth was just over 12 nm. Spectral broadening of the initial soliton pulse was created by SPM experienced in the amplifier. Using the spectral bandwidth and pulse width measured, the time-bandwidth product of the amplified soliton pulses was calculated to be 0.33. The Kelly sidebands were amplified more than the main lobe of the pulse, which became

modulated due to SPM. The amplified Kelly sidebands contained less than 20% of the average power.

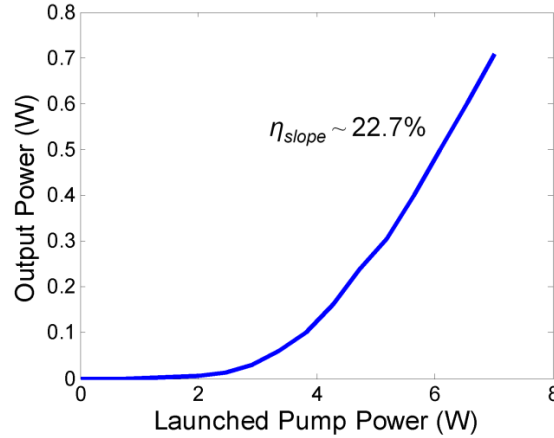


**Fig. 42.** Amplifier output power measured for increased launched pump power with soliton input pulses. At  $\sim 7$  W of pump power, the amplifier output more than 700 mW of average signal power with compressed pulses at a 10.4-MHz repetition rate.

The reconstructed pulse from the FROG measurement had a main lobe and two smaller side-lobes (see Fig. 43(b)), which contained less than 15% of the pulse energy. The temporal sideband pulse distortion is caused by SPM. Modulation of the pulse spectrum causes modification of the temporal pulse shape through the Fourier-transform relation. The energy in the main lobe of the pulse was  $\sim 50$  nJ. The full width at half of maximum of the reconstructed pulse in the FROG measurement in Fig. 43(b) was 370 fs, more than a factor of 4 less than the oscillator's output pulse width. The stretched pulse was compressed by a factor of 8 through the amplifier. After amplification, the peak power of the output pulse was around 115 kW, which created a nonlinear phase shift close to  $2\pi$  (and hence near the SPM threshold, see Eq. 5). The quadratic phase of the pre-chirped input pulse, which was introduced by the length of fiber between the oscillator and amplifier, was nearly compensated in the main lobe of the pulse by nonlinear chirp in the amplifier. This can be seen in the near-flat phase across the main lobe in Fig. 43(b).

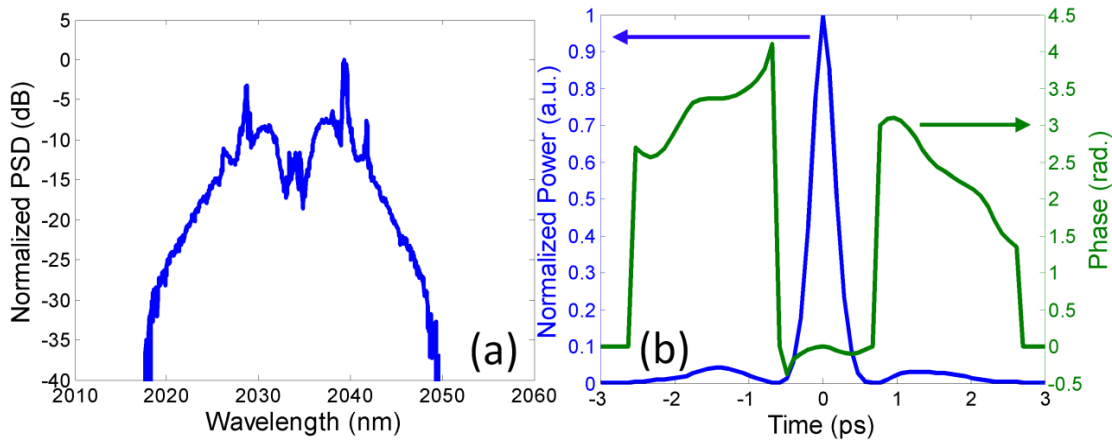


**Fig. 43.** Pulse characterization of the amplified soliton pulses from the F8L. (a) Normalized spectrum at the highest pump power. The outer 3-dB bandwidth of the output pulse spectrum was over 12 nm centered around 2035 nm. (b) The temporal reconstruction of the amplified pulse from the FROG measurement is shown for the maximum output power along with the estimated phase of the pulse. The reconstructed pulse width was 370 fs.

In the oscillator's square pulse regime, amplification through the same amplifier yielded  $\sim 1$  W of average output power. The longer, higher energy input pulses were able to extract more energy from the amplifier than the soliton pulses as expected, producing output pulse energies of  $\sim 100$  nJ. When using the soliton pulses, the amplifier is not saturated because the soliton's small input pulse energy ( $\sim 60$  pJ) cannot fully extract the stored energy within the amplifier. When using the square pulses with higher input energies ( $\sim 10$  nJ), more energy can be extracted from the amplifier as the higher input pulse energy can better saturate the amplifier. To fully saturate the amplifier and extract more energy with soliton pulses, a double-pass configuration could be explored. Another possibility would be to split the amplifier into two stages and create a preamplifier.

### Summary

The first Tm-doped all-fiber mode-locked F8L was modeled and demonstrated. Soliton pulses with 1.5-ps pulse width and 60 pJ of pulse energy were produced, which closely matched the simulated output. The oscillator could be tuned to produce square pulses of continuously adjustable widths—from  $\sim 100$  ps to 20 ns—with pulse energies of  $\sim 1$  nJ. Including both modes of operation, the output pulse width of the F8L can be varied to cover more than 4 orders of magnitude, from 1.5 ps to 20 ns. The performance of Tm-doped all-fiber lasers will continue to significantly improve as the quality and availability of 2- $\mu$ m fiber components advances.

With amplification, the soliton pulses from the F8L were compressed to pulses with a width of 370 fs, more than 12 nm of bandwidth around 2035 nm, and about 50 nJ of energy. When the F8L pump power was increased to produce square pulses of varying widths ( $\sim 100$  ps to 20 ns), these pulses were amplified to energies around 100 nJ. Including these two modes of operation, the output pulse width of the Tm-doped fiber laser system could be varied to cover more than 4.5 orders of magnitude, from 370 fs to 20 ns. Power scaling to much higher output pulse energies through a CPA system with a larger stretch and compress ratio is feasible.

## III. References

- [1] B.E. Carlsten, E.R. Colby, E.H. Esarey, M. Hogan, F.X. Kärtner, W.S. Graves, W.P. Leemans, T. Rao, J.B. Rosenzweig, C.B. Schroeder, D. Sutter, W.E. White, "New source technologies and their impact on future light sources," *Nuclear Instruments and Methods in Physics Research A* **622**, 657-668 (2010).
- [2] N. Leindecker, A. Marandi, R.L. Byer, K.L. Vodopyanov, "Broadband degenerate OPO for mid-infrared frequency comb generation," *Optics Express* **19** (7), 6296-6302 (2011).
- [3] D. Buccoliero, H. Steffensen, O. Bang, H. Ebendorff-Heidepriem, T.M. Monro, "Thulium pumped high power supercontinuum in loss-determined optimum lengths of tellurite photonic crystal fiber," *Applied Physics Letters* **97**, 061106 (2010).
- [4] P. Kadwani, J. Chia, F. Altal, R.A. Sims, C. Willis, L. Shah, D. Killinger, M.C. Richardson, "Atmospheric absorption spectroscopy using Tm: fiber sources around 2 microns," in *Atmospheric and Oceanic Propagation of Electromagnetic Waves V*, 22 January 2011, San Francisco, CA, paper 79240L.
- [5] M.A. Solodyankin, E.D. Obraztsova, A.S. Lobach, A.I. Chernov, A.V. Tausenev, V.I. Konov, E.M. Dianov, "Mode-locked 1.93  $\mu$ m thulium fiber laser with a carbon nanotube absorber," *Optics Letters* **33** (12), 1336-1338 (2008).
- [6] K. Kieu, F. W. Wise, "Soliton thulium-doped fiber laser with carbon nanotube saturable absorber," *IEEE Photonics Technology Letters* **21**, 128-130 (2009).
- [7] R.A. Sims, P. Kadwani, T.S. McComb, C.C. Willis, L. Shah, M. Richardson, "Fiber amplification of 2  $\mu$ m picosecond pulses," in *CLEO and QELS Conference*, 16-21 May 2010, San Jose, CA, paper CFK6.
- [8] R. C. Sharp, D.E. Spock, N. Pan, J. Elliot, "190-fs passively mode-locked thulium fiber laser with a low threshold," *Optics Letters* **21** (12), 881-883 (1996).
- [9] Q. Wang, T. Chen, K. Chen, "Mode-locked Ultrafast Thulium fiber laser with all-fiber dispersion management" in *CLEO and QELS Conference*, 16-21 May 2010, San Jose, CA, paper CFK7

- [10] M.A. Chernysheva, A.A. Krylov, P.G. Kryukov, E.M. Dianov, "Nonlinear Amplifying Loop-Mirror-Based Mode-Locked Thulium-Doped Fiber Laser," *IEEE Photonics Technology Letters* **24** (14), 1254-1256 (2012).
- [11] M.A. Chernysheva, A.A. Krylov, P.G. Kryukov, N.R. Arutyunyan, A.S. Pozharov, E.D. Obraztsova, E.M. Dianov, "Thulium-doped mode-locked all-fiber laser based on NALM and carbon nanotube saturable absorber," *Optics Express* **20** (26), B124-B130 (2012).
- [12] E.M. Dianov, "Fibre optics: Forty years laser," *Quantum Electronics* **40** (1), 1-6 (2010).
- [13] I.N. Duling, "All-fiber ring soliton laser mode locked with a nonlinear mirror", *Optics Letters* **16** (8), 539-541 (1991).
- [14] D.J. Richardson, R.I. Laming, D.N. Payne, V. Matsas, M.W. Phillips, "Selfstarting, passively modelocked erbium fibre ring laser based on the amplifying Sagnac switch," *Electronics Letters* **27** (6), 542-544 (1991).
- [15] M.E. Fermann, F. Haberl, M. Hofer, H. Hochreiter, "Nonlinear amplifying loop mirror," *Optics Letters* **15** (13), 752-754 (1990).
- [16] V. Tzelepis, S. Markatos, S. Kalpogiannis, Th. Sphicopoulos, C. Caroubalos, "Analysis of a Passively Mode-Locked Self-Starting All-Fiber Soliton Laser," *Journal of Lightwave Technology* **11** (11), 1729-1736 (1993).
- [17] G.P. Agrawal, *Nonlinear Fiber Optics* (Academic Press, 2001).
- [18] C.W. Rudy, K.E. Urbanek, M.J.F. Digonnet, R.L. Byer, "Amplified 2- $\mu$ m Thulium-Doped All-Fiber Mode-Locked Figure-Eight Laser," *Journal of Lightwave Technology* **31** (11), 1809-1812 (2013).
- [19] C.W. Rudy, M.J.F. Digonnet, R.L. Byer, S. Jiang, Q. Wang, "Thulium-doped Germanosilicate Mode-locked Fiber Lasers," in *FILAS Conference*, 1 February 2012, San Diego, CA, paper FTh4A.
- [20] S.M.J. Kelly, "Characteristic sideband instability of periodically amplified average soliton," *Electronics Letters* **28** (8), 806-807 (1992).
- [21] A.M. Weiner, *Ultrafast Optics*, 139-144 (Wiley, 2009).
- [22] M.F. Becker, D.J. Kuizenga, A.E. Siegman, "Harmonic Mode Locking of the Nd:YAG Laser," *IEEE Journal of Quantum Electronics* **8** (8), 687-693 (1972).
- [23] D.J. Richardson, R.I. Laming, D.N. Payne, V.J. Matsas, and M.W. Phillips, "Pulse repetition rates in passive, femtosecond soliton fiber laser," *Electronics Letters* **27** (16), 1451-1453 (1991).
- [24] B.J. Orr, *Infrared LIDAR Applications in Atmospheric Monitoring* (John Wiley & Sons, 2006).
- [25] D. Gay, A. Courmoyer, P. Deladurantaye, M. Briand, V. Roy, B. Labranche, M. Levesque, and Y. Taillon, "Micro-milling process improvement using an agile pulse-shaping fiber laser," in *Photonics North*, Quebec, Canada, 24 May 2009, paper 73860R.
- [26] D.J. Richardson, J. Nilsson, W.A. Clarkson, "High power fiber lasers: current status and future perspectives," *Journal of the Optical Society of America B* **27** (11), B63-B92 (2010).
- [27] P. Wan, L.-M. Yang, J. Liu, "156 micro-J ultrafast thulium-doped fiber laser," *SPIE Photonics West*, paper 8601-117 (2013).
- [28] J. Jiang, C. Mohr, J. Bethge, A. Mills, W. Mefford, I. Hartl, M.E. Fermann, C.-C. Lee, S. Suzuki, T.R. Schilbli, N. Leindecker, K.L. Vodopyanov, P.G. Schunemann, "500 MHz, 58fs highly coherent Tm fiber soliton laser," *CLEO* 2012, San Jose, CA, paper CTh5D.7 (2012).
- [29] F. Haxsen, D. Wandt, U. Morgner, J. Neumann, D. Kracht, "Pulse energy of 151 nJ from ultrafast thulium-doped chirped-pulse fiber amplifier," *Optics Letters* **35** (17), 2991-2993 (2010).
- [30] K.J. Blow, N.J. Doran, D. Wood, "Generation and stabilization of short soliton pulses in the amplified nonlinear Schrödinger equation," *Journal of the Optical Society of America B* **5**, 381-390 (1988).

## IV. Program Participants

Robert L. Byer	- Principal Investigator
Romain Gaume	- Research Scientist
Roger Route	- Senior Research Associate
Ye He	- Graduate Student Research Assistant
Charles Rudy	- Graduate Student Research Assistant

## V. Publications Supported Directly

A.P. Patel, M.R. Levy, R.W. Grimes, R.M. Gaume, R.S. Feigelson, K.J. McClellan, and C.R. Stanek, "Mechanisms of non-stoichiometry in  $\text{Y}_3\text{Al}_5\text{O}_{12}$ ", *Applied Physics Letters*, **93**, 191902 (2008)

J.A. Wisdom, R. Gaume and R.L. Byer, "Laser-gain scanning microscopy: a new imaging technique for engineered laser-gain media", *Optics Express*, Vol. **18**, Issue 18, pp. 18912-18921 (2010) doi:10.1364/OE.18.018912

R. Gaume, Y. He, A. Markosyan and R. L. Byer, "Effect of Si-induced defects on 1  $\mu\text{m}$  absorption losses in laser-grade YAG ceramics", *J. Appl. Phys.*, **111**, 093104 (2012)

J.A. Wisdom, R. M. Gaume, K. Urbanek, T. Plettner, R.L. Byer, A. Guichard, M.Brongersma, A. Kinkhabwala, W.E. Moerner, Akio Ikesue, Yan Lin Aung, "Characterization of a Nd:YAG Ceramic Laser with a 510- $\mu\text{m}$ -wide Engineered Doping Profile", in preparation.

C. W. Rudy, K. E. Urbanek, M. J. F. Digonnet, and R. L. Byer, "Amplified 2- $\mu\text{m}$  Thulium-Doped All-Fiber Mode-Locked Figure-Eight Laser", *Journal of Lightwave Technology*, Vol. **31**, Issue 11, pp. 1809-1812 (2013) doi: 10.1109/JLT.2013.2258891